UP500 Project
Report

A sensitive search for HI 21 cm emission from 'superdisks' in radio galaxies

Submitted in partial fulfillment of
the requirements for the award of the degree of

Master of Science
in
Physics

Submitted by
Abhijeet Anand
SR. No.- 11-01-00-10-91-12-1-10011

Advisor:

Dr. Nirupam Roy
Indian Institute of Science, Bangalore

Undergraduate Programme
INDIAN INSTITUTE OF SCIENCE
Bangalore - 560012, Karnataka

April 2017

Declaration

This thesis is a presentation of my original research work. The books, articles and websites, which I have made use of are acknowledged at the respective place in the text.

For the present thesis, which I am submitting to the institute, no degree or diploma or distinction has been conferred on me before, either in this or in any other institute.

Abhijeet Anand
Master of Science (5^{th} year)
(SR No. 11-01-00-10-91-12-1-10011)

Date:

Undergraduate Programme

INDIAN INSTITUTE OF SCIENCE, BANGALORE

Certificate

This is to certify that work contained in the thesis entitled **"A search for HI 21 cm emission from 'superdisks' in large radio galaxies"**, by **Abhijeet Anand** (Sr No.- 11-01-00-10-91-12-1-10011), has been carried out under my supervision during **Aug, 2016-March, 2017** in partial fulfilment of the requirements of the degree of **Master of Science** in **Physics**.

Dr.Nirupam Roy, IISc
(Project Supervisor)

Date:

To

all those who

do not lose hope

Acknowledgments

Firstly, I would like to express my deep gratitude to my project adviser Dr. Nirupam Roy of Indian Institute of Science, Bangalore. He consistently allowed this project to be my own work, and steered me in the right direction whenever he thought I needed it. Through out this project, he cleared all my doubts without any hesitation and motivated me to work hard. He helped me building an interest in this exciting field and provided all the scientific literature and resources required for this project.

I would also like to acknowledge Dr. Eric W. Greisen of NRAO for his continuous support through emails in the process of installing and learning the AIPS and CASA software that were required for this project work. I am also indebted to Dr. Prateek Sharma, IISc who provided me an advanced desktop where I performed all the analysis.

Finally, I must express my profound gratitude to my family and friends for providing me with unfailing support and continuous encouragement throughout my entire B.Sc (Research) - MSc course. This accomplishment would not have been possible without them. Thank you.

Abhijeet Anand
April, 2017
Indian Institute of Science, Bangalore

Abstract

The nature of ‘superdisks’ has been a major unknown even after detection of several disks in nearby radio galaxies. The proposed scenarios of these extremely large disks cannot be guaranteed until we directly observe them. The dusty material around the disk help reprocessing the high energy UV and X-ray photons to be emitted into radio or submillimeter range that can be detected by sensitive ground-based radio telescopes such as VLA and GMRT. These emission can provide some invaluable information about the intrinsic structure of these disks in way that has never been tried. In this effort to understand the nature of superdisk we have observed 4 nearby radio galaxies (with known superdisks) namely 3c98 ($z = 0.030$), 4c+32.25 ($z = 0.0512$), 3c192 ($z = 0.0597$) and 3c227 ($z = 0.0858$) with VLA for a sensitive search for H I emission. Due to limited time given on telescope and after the removal of RFI we have not detected any emission on the calibrated data within the velocity width of 100 km s^{-1} but we report the the upper limit on H I mass to lie between $4.2 \times 10^8 - 5.41 \times 10^9$ $M_\odot$ in 3σ rms noise limit. These masses are quite comparable to total H I content in our Milky Way galaxy. We also report the upper limit of H I number density lying in the range of $10^{-4} - 10^{-3}$ atoms per cm^3 and the column density in the range of $10^{19} - 10^{20}$ atoms per cm^2 in the same noise limit, which is quite small in comparison to normal galaxies because of extremely large nature of these disks. These values are strong upper limits on H I mass, H I number density and column density. The low H I number density and intermediate column density very strongly indicate that most of the gas in ‘superdisk’ is in the ionized or molecular form or a mixture of them with this little amount of neutral hydrogen. This also suggests the possibility of some other large-scale structure that we still don't know. It would be exciting to observe some more RGs with ‘superdisks’ to answer this question.

Contents

List of Figures

List of Tables

Chapter 1

Introduction

1.1 Galaxies

The night sky is full of tiny twinkling dots (stars) that make an amazing and breathtaking view for us, however if we see more carefully we find that stars are not distributed very uniformly. We can see some faint and huge cloud of light spreading over large distances in the sky, these are galaxies. Each galaxy contains billions of stars that are gravitationally bound with each other that prevent them from random motion. In normal galaxies (see next sections for radio galaxies) almost all light is emitted by its stars. This composite light can provide some invaluable information about the structure and morphology of the universe. In 1920, galaxies were morphologically classified based on their appearances through optical telescopes. This divided galaxies in three different morphology classes - *spiral*, *elliptical* and *irregular*.

The *spiral galaxies* have a characteristic circular disk (spiral arms) with a central bulge (see Figure 1.1a). The spiral arms are star forming regions because they contain considerable amounts of interstellar dust and therefore look brighter than the surrounding disk. This combination of circular disk and central bulge is surrounded by faint halo of stars that reside in globular clusters. The Milky Way and near by Andromeda Galaxy are two very famous examples of spiral galaxy[5].

The other class is of *elliptical galaxies* (see Figure 1.1b) that have ellipsoidal shape and do not have any special features apart from their different ellipticities. It is very hard to deduce the absolute ellipticities from the apparent shapes of these galaxies, but still they are subclassified based on their apparent shapes in the sky from almost circular looking to flattened elliptical. In contrast with spiral galaxies, elliptical galaxies contain fairly less amount of ISM and star formation is considerably less hence most of the stars are quite old and the galaxy looks more yellowish whereas spiral galaxy appears bluish because of young stars. The size of elliptical galaxies can be much larger than spiral galaxies (can be smaller also, dwarf galaxies), for example the diameter of giant elliptical galaxy NGC 1132 is about 80 kpc while milky way has a diameter of about 30 kpc[5].

Apart from these well defined shapes, there are some galaxies which do not fall in any of these categories and have very irregular shapes, they are classified as *irregular*

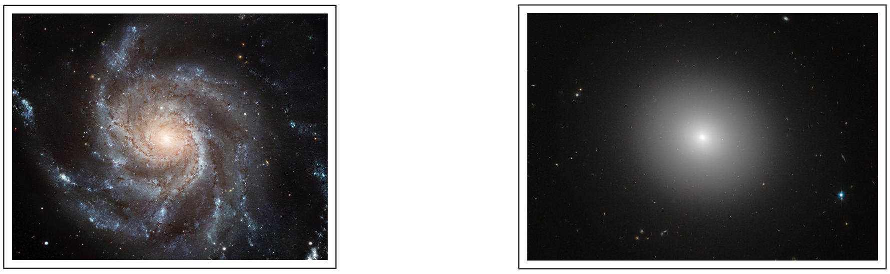

(a) face-on spiral galaxy M101 (b) elliptical galaxy IC 2006

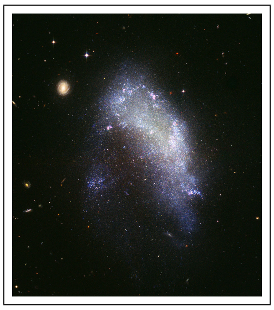

(c) irregular galaxy NGC 1427A

Figure 1.1: Classification of galaxies (Ref: wikipedia)

galaxies (see Figure 1.1c). They may contain enough interstellar dust to trigger the star formation. In the next section we will focus on our own galaxy Milky Way to give a flavour of some typical numbers for mass, diameter and angular speed[5].

1.1.1 Milky Way

Our galaxy is one of the billions galaxies in universe, so nothing special here. The Milky Way is an intermediate size spiral galaxy with its characteristic flat disk and central bulge. Alike, other galaxies it also contains stars, gas and dust. An external observer might see the Milky Way looking something like shown in Figure 1.2. The sun lies nearly halfway in the disk from the center. The disk is thin and roughly circular and the stars residing there appear as a luminous band stretching across the sky in night. The dust and gas look as dark (darkness proportional to concentration) patches in this luminous band. The central bright region (the bulge expanding above and below the disk) can be seen in the southern sky. The detailed studies of the dynamics of stars in the central region (nucleus) confirms the presence of a supermassive black hole with mass, $\mathrm{M_{BH}} \approx 4.1 \times 10^6 M_\odot$. Astronomers prefer to measure the distances in *kiloparsecs (kpc)* within the galaxy. Mathematically, 1 $kpc = 10^3$ $pc = 3.086 \times 10^{16}$ km. The other commonly used units are *megaparsecs (Mpc)* and *gigaparsecs (Gpc)*. The radius of bulge is about 1-2 kpc and the disk stretches out to at least 15 kpc with sun lying at around 8 kpc from the center. The rough estimate of number of stars is about 100-400 billion in Milky Way with a mean separation of 5 ly ($\sim$1.5 pc) between them. Most of these stars ($\sim$ 95%)

reside in thin disk (thickness $\sim$ 0.6 pc) and they are young and massive. The number density of stars falls of exponentially by a factor of $1/e$ when moved by a distance of about 2.5 – 4.5 kpc in the plane of the disk, and this length is called, *scale length, h_R.* The gas and dust lie in midplane (near to sun) in a thin layer with most of the hydrogen gas lying within 100 pc, obscuring most of the light from the central bulge[11].

The disk and bulge are not static, in fact, they are differentially rotating. The stars residing in the disk orbit (in nearly circular orbits) the galactic center with 200 km s^{-1} so the sun takes 250 Myr to complete one orbit. The stars and globular clusters present in **halo** do not have well defined orbits around the center of galaxy and they often rotate in eccentric orbits in random directions. These globular clusters and stars are very old and provide us the invaluable information about the evolution of our galaxy. The total luminosity of the disk is about (15–20) $\times 10^9 L_\odot$ and total mass of stars is $60 \times 10^9 M_\odot$. In the central bulge the luminosity is about $5 \times 10^9 L_\odot$ and stars' mass is $20 \times 10^9 M_\odot$. The halo mass is a very small fraction of these masses and is less than $10^9 M_\odot$. Mathematically, total mass of the galaxy is more than the combined mass of stars and gases and we call this extra mass as *dark matter* and assume it to lie in the *dark halo.* About 90% of halo's mass comes from the dark matter. The ongoing research to unveil the dark nature of this matter is a very hot topic in the field of astronomy. The typical diameter of stars is about 10^{-7} pc but the mean distance between stars is about 1.5 pc that implies that most of the interstellar space is devoid of stars. The study of emission and absorption of light from ISM itself is a big field of research and provides us crucial information about the star formation[11].

1.1.2 Radio Galaxies

As we have discussed in above sections that most of the emission in a galaxy is due to the stars and gas, but there are galaxies that host an *active nucleus* which is a compact central region (dimension of only few parsecs) and emits substantial emission which is not starlight or emission from gas. The emission is quite strong over all electromagnetic spectrum including high energy regions (x-ray, γ-ray). The normal galaxies hardly radiates in high energy regions. The most powerful among these are *quasars* that easily outshine their host galaxies. The high luminosity of $10^{13} L_\odot = 10^{46}$ erg s^{-1}, makes them bright enough to be visible through a very large distances ($\sim$Gpc) in the observable universe thus make them as invaluable tools to peep back into the time. The emission is thought to be due to the falling gas into the central black hole. The shape of radio-frequency spectra indicates that emission is non-thermal in origin and assumed to be due to synchrotron radiation from relativistic electrons with energy upto 1 GeV moving in relatively weak magnetic field of strength 10^{-4} G[29].

The radio galaxies are also active galaxies and as the name suggests they are very luminous in radio wavelengths. The luminosities may vary somewhere in the range of 10^{41} to 10^{46} erg s^{-1}. The radio maps of these objects show a wide range of structures, most common are the oppositely directed **jets** coming from active nuclei and **lobes** (mostly symmetric but sometimes asymmetric, ellipsoidal in shape located where jets are finally stopped by intergalactic medium) present on either side of the nucleus. The host galaxies

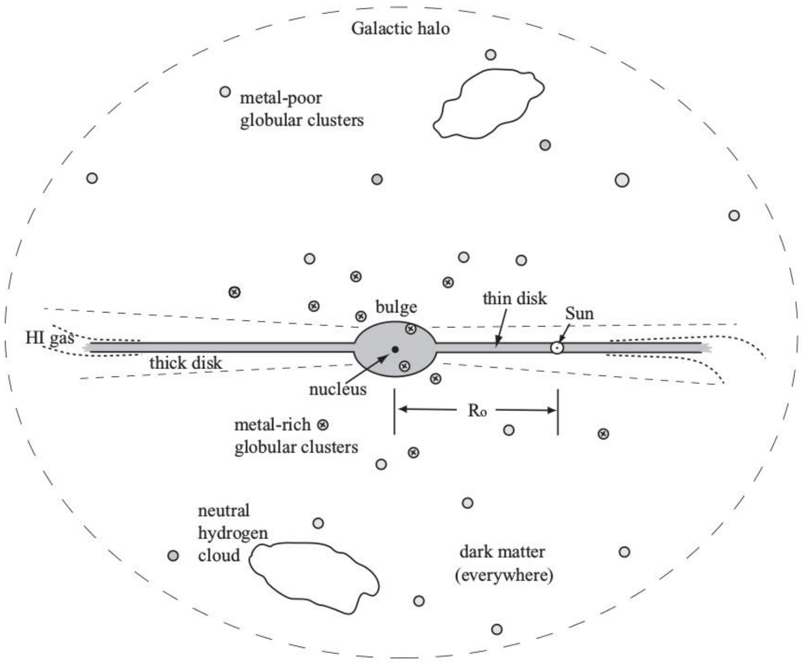

Figure 1.2: A schematic side view of Milky Way from an external observer[11]

of these nuclei are almost always (but with some exceptions) the large elliptical galaxies. The radio emission from jets and lobes is probably due to synchrotron radiation, as the emission spectra fits very well to the characteristic power-law spectra of synchrotron radiation. In very bright radio sources (like quasars) narrow twin relativistic radio jets can go up to several kpc or Mpc away from the central source. It seems the energy, the magnetic fields, relativistic particles and probably the thermal gas are being taken out from the nucleus to form these extended jets.

Based on the host-galaxy environment and hence the morphology of large-scale radio emission the radio sources were divided into two classes known as - FR I and FR II[1]. There is a sharp line between the luminosities, FR I is limb darkened (brightness goes down as we move away from the nucleus) and less luminous and FR II is limb-brightened away from the nucleus and more luminous. FR II often have small '**hotspots**' at the farthest edges of lobes or sometimes may apparently be embedded in the diffuse structure[29]. A false color image of a typical radio galaxy (FR II class) can be seen in Figure 1.3. In next sub sections we will give some more details of the properties, spectra and energy scales of these galaxies.

---

[1] FR abbreviates to Fanaroff and Riley who first defined these classes in 1974.

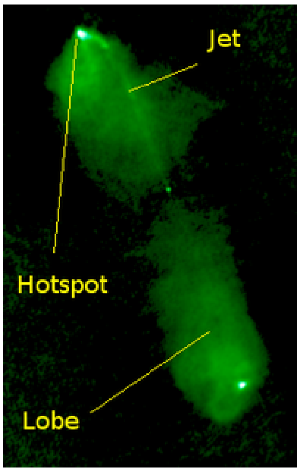

Figure 1.3: False-color image of FR II radio galaxy 3c98 (Ref: wikipedia)

1.1.2.1 Radio Source Properties

As discussed above one very characteristic feature of the radio-frequency spectra is its power law shape similar to synchrotron radiation. The ultra-fast moving ($\gamma \sim 1000$) electrons in magnetic field of strength $10^{-4} - 10^{-5}$ G is the source of this synchrotron radiation. Based on the electron density the radio emission can be divided into two categories: *extended* (lobe-dominated) and *compact* (core-dominated). The extended structure is almost *transparent* to its radiation as electron density is considerably low, whereas compact structures are almost *opaque* to its own radiation because of extremely high electron density in them. The typical radio source dimension varies from 10 kpc to few Mpc with nuclei size ranging from 1 to 100 kpc[29].

1.1.2.2 Radio Spectra

In order to develop broadband spectra (emission in wide range of radio wavelength) of radio galaxies we need to combine the data from several radio telescopes (every telescope works with limited radio wavelength range). This combination of data requires to calibrate every telescope at each observed wavelength (see Ch-2 for more detail). Several radio galaxies have been observed for these purpose and a complete spectra over a large frequency range (10 MHz to 100 GHz), above this range the observation is extremely difficult as high frequency radio waves are stopped by earth's atmosphere. The radio spectra is typically presented in log-log plot of flux versus frequency. The characteristic feature of power law spectrum appears as straight line in this plot[29].

1.2 Why should we study radio galaxies ?

As we have mentioned in above sections that due to their powerful emission they can be used to look back into the time and can provide us invaluable information about the evolution of universe. The bright emission lines of radio galaxies make easier to find their redshifts and indeed the most distant objects with very high redshifts are radio galaxies. Therefore the observation of several radio galaxies and selecting distant galaxies based on their radio spectrum has helped astronomers to find objects at high redshifts. The radio jets penetrate through the diffuse external medium in the process of expansion hence they are required to perform huge amount of work that can only be stored in the nuclei and lobes. The largest known physical structures in universe are often constituted by some extended radio sources and they can have very high energy content upto 10^{60} ergs or more. The deep understanding of this huge energy generation can provide crucial information about the mechanism of energy generation in such exotic objects and would reveal mysteries of formation of other massive objects[29].

1.3 Role of Neutral Hydrogen

Hydrogen is one of the most important and abundant elements in universe. The collapse of high concentration of H I clouds sets the stage for star formation. Galaxies abundant in H I indicate high rate of star formation whereas lacking H I almost guarantees no star formation. The H I plays a pivotal role in the structure and evolution of galaxies. For example, in Milky Way (which is an intermediate-to-late type spiral) most of the H I reside in periphery of the disk or in the envelopes that surround the molecular gas. The total mass of atomic hydrogen in our galaxy is few times $10^9 M_\odot$ [29].

1.3.1 H I 21 cm line

From the above discussion it is clear that H I can be a very important tool to study the structure, dynamics and evolution of the galaxy. The reason behind this importance is the ease of detection (with radio telescopes) and its reliability in finding the column density and other parameters such as mass.

In the ground state of neutral hydrogen depending upon the parallel (triplet) or anti-parallel (singlet) nature of electronic and nuclear spin the energies of magnetic dipole can be different this is called the hyperfine levels. The transition between these two magnetic dipole energy levels leads to the emission of 21 cm photons that come under radio band of electromagnetic spectra and can easily be detected by ground based radio telescopes. The atmospheric opacity is almost transparent to these waves. The H I can provide many invaluable information such as quantity of interstellar H I, excitation temperature and radial velocity from Doppler shift. In the next sub section we will give a brief mathematical illustration of H I 21 cm photon emission. See Figure 1.4 for pictorial representation of the 21 cm emission.

1.3.2 Mathematical Description

In hydrogenic model of atom the nucleus can be thought as a single particle with spin $\vec{I}$, called nuclear spin. The magnetic dipole moment of nucleus is quite smaller than the electron due to its heavy mass. The magnetic dipole moment of nucleus (assuming hydrogen atom) is given by -

$$\tilde{\mu}_{\mathrm{p}} = \frac{\mathrm{g_p}}{2\mathrm{m_p c}}\tilde{\mathrm{I}} \tag{1.1}$$

where g_p is nuclear g-factor and m_p is nuclear mass. There will be magnetic field $\vec{B_p}$ due to proton and electron will have a potential energy, $U = -\vec{\mu_e} \cdot \vec{B_p}$ in this field. This potential energy can be treated as a perturbation in the Hamiltonian of the ground state of hydrogen and depending upon the spin arrangements, the first order energy correction can be calculated using standard techniques of time-independent perturbation theory. The energy difference due to this parallel or anti-parallel nature of magnetic dipole in hydrogen atom (spin of proton and electron is $\frac{1}{2}$) is given as -

$$\Delta\mathrm{E} = \frac{4\mathrm{g_p}\hbar^4}{3\mathrm{a_o m_p m_e^2 c^2}} \tag{1.2}$$

Putting the typical values for these quantities for hydrogen atom with $g_p = 5.56$, we get -

$$\Delta\mathrm{E} = 5.88 \times 10^{-6}\ \mathrm{eV} \Rightarrow \nu = \frac{\Delta\mathrm{E}}{\mathrm{h}} = 1420.4\ \mathrm{MHz} \Rightarrow \lambda = \frac{\mathrm{c}}{\nu} = 21.1\ \mathrm{cm} \tag{1.3}$$

This wavelength corresponds to radio wavelength and is the famous H I 21 cm line.

1.3.3 H I Mass Estimation

This 21 cm line can effectively be used to calculate the H I mass in extrgalactic objects, if assumption of optically thin ($\tau \ll 1$) emitting region can be hold. The observed flux in 21 cm line can be calculated as - $F_{obs} = \int F_\nu d\nu_{obs}$, where F_ν is the observed flux density which will be redshifted as - $\nu_{obs} = \frac{\nu_o}{1+z}$, where z is the redshift of the galaxy. In radio astronomy, the integrated flux is typically reported in 'Jy km s^{-1}' unit and $d\nu_{obs} = \frac{\nu_o}{1+z}\frac{dv}{c}$. Finally the H I mass is given as [9] -

$$\mathrm{M_{H\,I}} = 2.343 \times 10^5 (1+\mathrm{z}) \left(\frac{\mathrm{D_L}}{\mathrm{Mpc}}\right)^2 \left(\frac{\int \mathrm{F_\nu dv}}{\mathrm{Jy\ km\ s^{-1}}}\right)\ \mathrm{M_\odot} \tag{1.4}$$

where, D_L is the luminosity distance to the source.

1.4 Superdisks

With increasing number of observation of radio galaxies and their optical imaging surveys, it has been revealed that the presence of dust lanes or dusty patches can be a very generic feature of radio galaxies (RGs) (Goudfrooij 1994; also de Koff et al. 1996; McCarthy 1996). The emission of non thermal radio emission from the active nucleus of elliptical galaxy is triggered by the accretion of gas-rich disk by that galaxy (Sparks, Macchetto & Golombek 1989; Ellingson, Yee & Green 1991; Colina & de Juan 1995). Therefore with the assumption that the past universe hosted a large number of such accretion events the

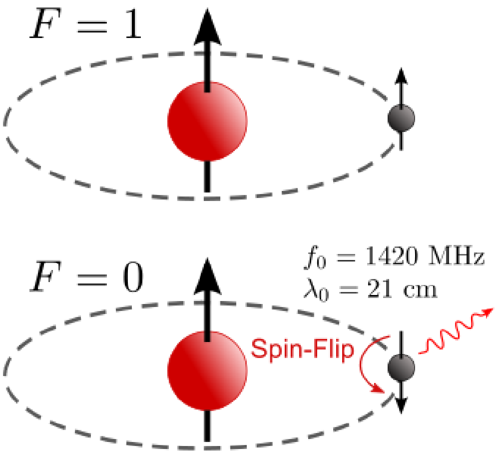

Figure 1.4: Magnetic dipole transition in neutral hydrogen in ground state (Ref: wikipedia)

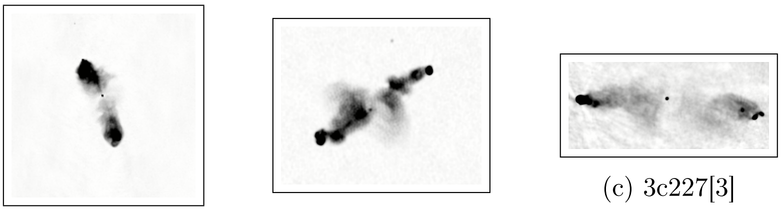

(a) 3c98[1]

(b) 3c192[2]

(c) 3c227[3]

Figure 1.5: VLA radio images (Ref: NASA Extragalactic Database)

study of such dust lanes in RGs at high redshifts becomes important. The high quality images (in radio and Ly-α) of some FR II RGs have revealed the presence of very large disks with diameter greater than 75 kpc and thickness $\sim$ 25 kpc that sharply separate the radio lobes. Such large disks are much greater than the dust lanes found in nearby RGs (Gopal-Krishna & Witta 2000). These large disks are called 'superdisks'. The standard models of jets and lobes predict the backflow of some of the synchrotron plasma (that is deposited in hotspots) into the lobes surrounding the jets (Scheuer 1974; Blandford & Rees 1974). In typical RGs this backflow has a very complex flow pattern where material closest to the jets is usually dragged in forward direction but the material far from jets still flows backward toward the ISM of the galaxy (Clarke 1996; Norman 1996; Hooda & Wiita 1996, 1998), but if the medium is quite denser (than the ISM) these backflows can be sharply stopped (as their speed is only about $\sim$30% of the forward flow) and this blocking will give rise to emission gap between two lobes (Leahy & Williams 1984; Leahy & Perley 1991). See Figure 1.5 for sharp wide radio gaps.

1.4.1 Evidences of 'superdisks'

Previously these sharp blocking (radio gaps) of the back-flowing synchrotron plasma in radio lobes were interpreted as due to ISM of the host galaxy but the gaps are too wide to be accounted by ISM. With the help of high quality radio and optical observations we are led to believe toward the existence of extremely large gaseous disk-like structures that stops these backflows.

1.4.1.1 Radio Evidence

The key evidence for this sharp boundary (formed due to blockage of backflows by these disk-like structure) comes from the detection of conspicuous emission gaps with quasi-linear edges in the middle of the radio lobes in powerful double radio sources (see Figure 1.5). If we carefully observe the radio maps the linear extent of the sharp boundaries of the radio lobes and gaps between the lobes can provide us invaluable information about the lower limits of the diameter and thickness of the postulated superdisks. The radio maps of 12 nearby ($0.03 \leq z \leq 0.09$) powerful RGs estimate the median disk diameter to be ~ 75 kpc (lower limit) and thickness to be ~ 25 kpc (lower limit) (Gopal-Krishna & Wiita 2000). The radio maps are quite reliable and useful for nearby RGs, but they become a weak tool to study for such disks in high- z RGs, because first they need to be very luminous in radio to be observed and second their surface brightness is strongly affected by cosmological dimming making it difficult to be observed. But this can be circumvented by optical surveys.

1.4.1.2 Optical Evidence

The detection of Lyα emission ($\lambda \sim 1216$ Å) is an important tool in astronomy to study interstellar dust. The highly extended ($\sim 10-100$ kpc) Lyα emission line is a prominent feature of most of the powerful radio galaxies (Spinrad 1989; McCarthy 1993). The Doppler shifting of Lyα emission allows it to fall in optical band for $z > 1.8$ making them to be detected by ground-based telescopes. With several optical maps of high-z RGs the geometry of dust distribution can be inferred with their Lyα images, where emission looks distinctly asymmetric about the active nucleus (Gopal-Krishna et al. 1995). Several RGs at high redshifts have been observed showing substantial Lyα emission asymmetries such as: 3c294 ($z = 1.82$, McCarthy et al. 1990), 3c326.1 ($z = 1.82$, McCarthy et al. 1990), 1243+036 ($z = 3.57$, van Ojik et al. 1996). The observed asymmetry in Lyα emission is due to obscuring of Lyα photons (arising from farther side of nucleus) by large disks that is surrounding the host galaxy.

1.4.2 Importance of 'superdisks'

The presence of superdisks can provide very plausible explanations for some important phenomena namely, Laing-Garrington effect (where lobe on the side of jet depolarize less than the opposite lobe)(Laing 1988; Garrington et al. 1988; Garrington, Conway & Leahy 1991). The requirement of the original explanation is very well satisfied by these large disks. The correlated radio-optical asymmetry for FR II radio galaxies can also be explained by superdisks and have been dealt in detail in (Gopal-Krishna & Wiita 2000). The other important role superdisks can play in relation to the large multiple dips in the Lyα emission profile of high redshift RGs (Gopal-Krishna & Wiita 2000).

1.5 Our Aim

In above sections we have discussed observational evidences, importance and size of superdisks, but still we could not answer one of the most fundamental question about them and it remains a major unknown. This makes us curious to focus on their nature and origin. There are some proposed scenarios for superdisks, but they cannot be guaranteed unless we directly observe them. The dusty material of superdisk can easily reprocess the high energy UV and X-ray emission from the active nuclei into far-IR or submillimeter range that can be detected by ground based radio telescopes. The nearby powerful RGs with luminosity of about 10^{45} erg s^{-1} can be very suitable candidate for this direct observation of superdisk because even if the disk can reprocess 1% of this emission the re-radiated photons it can be detected by large baseline radio telescopes (such as VLA, GMRT) (Gopal-Krishna & Wiita 2000). In this effort to understand the nature of superdisk we have observed 4 nearby radio galaxies (with known superdisks) namely 3c98 ($z = 0.030$), 4c+32.25 ($z = 0.0512$), 3c192 ($z = 0.0597$) and 3c227 ($z = 0.0858$) with VLA for a sensitive search for H I emission. The detection of H I 21 cm emission will help estimating the neutral hydrogen distribution in the superdisk and can be compared with normal galaxies' H I content. Theoretical calculations predict the masses to lie in the range of few billion solar masses comparable to H I content in normal galaxies like Milky Way. Even the non detection will be much rewarding because it would allow us to put a more stringent limit on the distribution of H I gas in the superdisk. In the subsequent chapters we will discuss our data analysis techniques and the obtained results.

Chapter 2

Data Analysis

With a brief introduction and scientific motivation of 'superdisks' in previous chapter we will now discuss the data acquisition and its analysis in detail in this chapter. We have analysed the VLA data of four large nearby ($0.03 \leq z \leq 0.09$) radio galaxies namely 3c98, 3c192, 4c+32.25 and 3c227 to search for the H I 21 cm emission from the 'superdisks' around these galaxies.

2.1 Data Acquisition

The above mentioned nearby radio galaxies were observed with Very Large Array (VLA) (see Figure 2.1), Socorro, New Mexico of National Radio Astronomy Observatory during Jan - Mar, 2013 by Dr. Nirupam Roy. The observations were designed to take data in order to search for the H I 21 cm emission in the continuum emission gap region arising from the plausible superdisk in such systems. The first three sources (3c98, 3c192, 4c+32.25) were observed for 1.5 hrs each and the last source (3c227) with highest redshift, z = 0.0858 for 4 hrs. In fact, 3c227 was observed on two different days one in Jan, 2013 and on Mar, 2013 for 2 hrs on each day. With calibration and other overheads the total time spent at VLA for the observations was 11 hrs.

2.1.1 Technical Details

With theoretical calculations based on telescope resolution, source size, distance, velocity dispersion and observational evidences at the redshifted H I frequencies the expected rms noise is about 1.12 - 1.22 mJy per 10 km s^{-1} spectral channel in 1 hr on source integration time with the VLA. The theoretical calculations also suggest that with the above mentioned observation duration the 5σ detection limit can be achieved. This implies that the H I mass can lie in the $1.2-6.6\times10^{9}M_{\odot}$ range. The radio signals coming from distant objects are very weak compared to signals emitting from communication devices and can severely be swamped by these strong signals. This is called Radio Frequency Interference (RFI). In reality, RFI is almost always present and will deviate

Figure 2.1: Arial view of Very Large Array (VLA), Socorro, USA (Ref: `http://www.aoc.nrao.edu/epo/puente/views/vlaviews.index.html`)

the observational data from the theoretical predictions. In presence of RFI the above mentioned numbers can slightly vary and can go up to $1.5 - 8.5 \times 10^9 M_\odot$.

There are two subbands that were simultaneously used for these observations. The first subband called **spw0** was centered at the respective redshifted H I frequencies of each source and sub-divided into 128 channels of width 1000 kHz each giving a broader bandwidth of 128 MHz. The other subband called **spw1**, centred again at the respective H I frequencies, but sub-divided into 512 channels of width 31.250 kHz each, constructing a narrow bandwidth of 16 MHz. This subband would provide a total velocity coverage of ~ 3500 km s^{-1}. The reason that we observed the sources in two subbands was to enhance our ability to image and subtract the continuum.

2.1.2 Details of Observed Radio Galaxies

In this sub section we will give some observational details of the sources that we observed with VLA. As we have discussed in Ch-1 the radio observation will be helpful for nearby radio galaxies so the chosen candidates are low-z RGs with known superdisks. The following tables summarize the basic parameters of these radio galaxies.

Table 2.1: Parameters of the observed radio galaxies

Source	**RA**	**DEC**	z
3c98	$03^h58^m54^s$	$10^h26^m03^s$	0.0304
4c+32.25	$08^h31^m27.5^s$	$32^h19^m26^s$	0.0512
3c192	$08^h05^m34.9^s$	$24^h09^m50^s$	0.0597
3c227	$09^h47^m45^s$	$07^h25^m20^s$	0.0858

Table 2.2: Continued....

Size (arcsec)[14]	**Time on source (hr)**	**total time (hr)**	ν_{mean} **(MHz)**
30	1.5	2	1378.34
307	1.5	2	1351.16
190	1.5	2	1340.37
230	4	5	1308.15

2.2 VLA Data Reduction Steps

In this section we will give the detail of data analysis that we performed to search for the H I emission from the superdisks. The data analysis steps are standard one that are typically used for such systems to extract the emission after subtracting the continuum part. The analysis part is quite tedious and time consuming and should be done with a great care in order to reach the scientific goal. We have used the standard VLA data analysis software packages such as Common Astronomy Software Applications (CASA) and Astronomical Image Processing System (AIPS) that are developed by NRAO.

There are certain steps which are to be followed before we perform actual imaging to get the maps and spectrum. These are initial flagging and calibration steps. In the following subsections we will illustrate each step in detail with examples from our analysis.

2.2.1 Flagging

As we have mentioned above that the incoming radio signals can be affected by many things. Therefore it becomes important to check these bad signals such as RFI and remove them before we create the radio maps. The noise due to these unwanted signals can be so high that it would subsume our real signals. The CASA task **plotms** and AIPS task **uvplt** were used for this purpose. These both task can plot a wide variety of parameters for different spectral windows, channels and fields (observed objects) in order to search for any bad signals in data. A pair of antennas (called interferometers) measures one point (signal) in u-v plane (see Figure 2.2). Mathematically, a useful vector called, 'uvdist (**uv**)' is defined as the vector sum of u-v coordinates **u** (east - west direction) and **v** (north - south direction).

$$\mathbf{uv} = \mathbf{u} + \mathbf{v} \Rightarrow |\mathbf{uv}| = (|\mathbf{u}|^2 + |\mathbf{v}|^2)^{\frac{1}{2}} \tag{2.1}$$

The sky plane ($l,\ m$) and u-v plane are mathematically related through Fourier Transform ($\mathcal{F}$) as-

$$(u, v) \xrightarrow{\mathcal{F}} (l, m) \tag{2.2}$$

and, the dependence becomes reciprocal to each other as - $u \propto \frac{1}{l}$ and $v \propto \frac{1}{m}$.

One very useful way to find the unwanted spikes that could arise due to RFI is to plot *amp vs. time* or *amp vs. uvdist.* These two plots can help us finding bad data immediately and the interactive mode of CASA and AIPS would allow us to flag the unwanted signals. The first plot would show us the amplitude of signals (for each fields-source + calibrators) received by the antennas as a function of observation time (see Figure). The spikes or unwanted signals can easily be removed with these tasks[30]. It would also let us know if some antennas were not working at the time of observation and did not receive any signals and should be eliminated from our data set. There are certain source structures that we know based on several radio observations such as constant amplitude structure for point sources, exponentially decaying signals (highest signals at lower baselines and lowest signals at higher baselines) that can help identifying bad data. However, there may be sources for which the structure is unknown and that require a more careful analysis for flagging. The sources can be more extended in one direction than other and can be seen by plotting (inverse proportionality ensures maximum signal for lower baseline either in north-south or east-west direction) signal amplitude with u-v coordinate. In our case, the source 3c227 has this feature where it is more elongated in east-west direction (u) than the north-south (v).

In CASA the most useful task for flagging bad data is **flagdata** that allows us to perform flagging through interactive mode. The Figure 2.3 shows the data before and after flagging. We can easily see that unwanted spikes due to RFI or other interferences can easily subsume our original signals. The figure 2.3d shows the exponentially decaying source structure.

2.2.2 Calibration

Once we have removed the bad data from our measurement set, the next step is - calibration. Alike any experiment here too we need to calibrate our instrument (as a whole or its separate component) and data. The radio data must be calibrated to correct for the effects that may interfere with the scientific outcome of a measurement (an observation) due to the instrument and local temporary conditions so that these measurements can be compared to other measurements (at other times, other instruments, other frequencies, etc.) and theoretical predictions. The amount of calibration depends on the observation program and scientific goal so calibrators are selected in accordance to them. There are some calibrations for which the solutions are typically constant over time, hence they are performed just once during the observation, however, some need to be performed

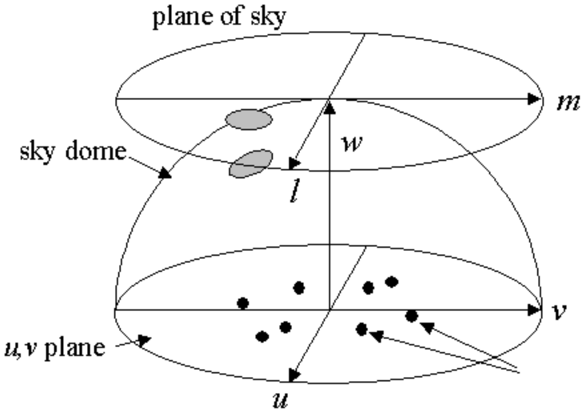

Figure 2.2: A schematic of u-v plane [34].

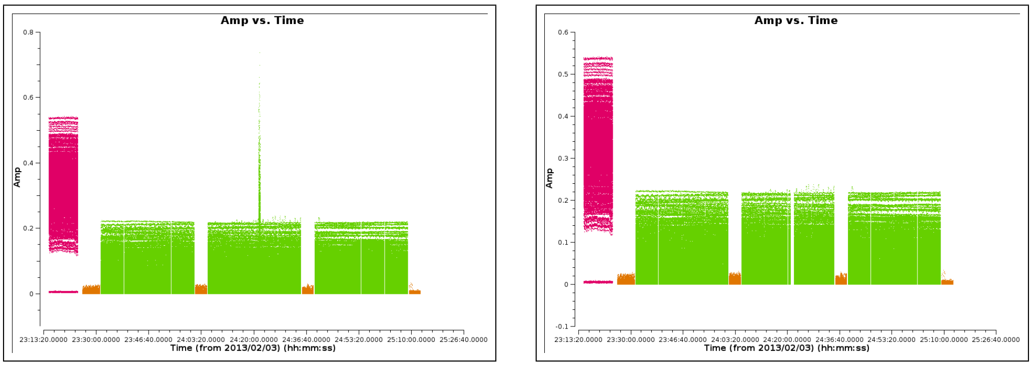

(a) Unflagged data with RFI spikes

(b) Flagged data

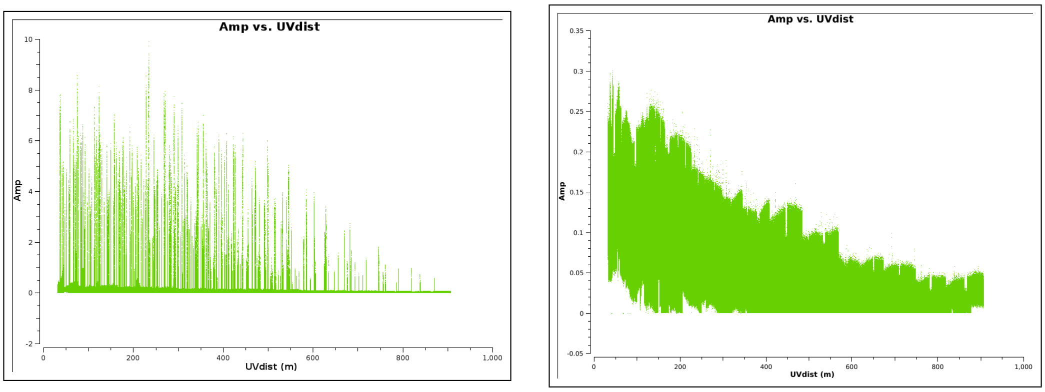

(c) Amplitude with RFI spikes

(d) Flagged amplitude

Figure 2.3: 3c98 data before and after flagging.

repeatedly to capture their time varying properties. The general strategy of calibration is to derive a chain of scaling and corrections and then collectively apply to the science data. In most cases, we follow some common steps listed below -

- Instrumental calibrations that correct the antenna for receiver frequencies, receiver system temperatures, optics, antenna positions, timing and correlator visibilities.
- Calibration for instrumental delay, spectral bandpass response and absolute flux density scale that typically remain constant over time. These are done by observer once or twice during the entire observation for each observed frequency and correlator configuration.
- Calibration for rapidly varying properties like antenna gains, atmospheric phase fluctuations which depend on observing condition and local antenna geometry during observations, is done frequently than the time scale over which these properties change.
- Calibration for slowly varying properties like antenna pointing, attenuator response and response of noise shaping requantizer is done less frequently like every hour or so during the observation.
- Above calibrations are mostly instrumental (directly or indirectly) but we need to calibrate our data also, hence the calibration of position of target source w.r.t other source (for which the position is known accurately), calibration of a frequency to line-of-sight velocity, calibration of the flux density scale of a single source in one observation to another observation of the same source, etc are done for this purpose.

In summary, mathematically the calibration can be understood in one equation. The whole effort is made to find the parameters that connect the observed (V_{obs}) and true visibilities (V_{true}). The mathematical relation between two is -

$$\mathrm{V_{ij}(u,v,t,\nu)_{obs} = b_{ij}(t)[B_i(t,\nu)B_j^*(t,\nu)]g_i(t)g_j(t)V_{ij}(u,v,t,\nu)_{true}e^{i[\theta_i(t)-\theta_j(t)]}} \tag{2.3}$$

where, $g_i(t)$ and $\theta_i(t)$ are the amplitude and phase part of complex gain and $B_i(t,\nu)$ is complex bandpass that incorporates the frequency dependent response of instrument. In most cases, $b_{ij}(t)$ (baseline term) can be neglected.

Now a very natural question arises - when should we perform these calibrations? The answer is quite simple, before the property changes to an extent that it can not be compensated for. The calibration for almost constant properties can be performed in start or end of the observation. The changes in time varying and geometry dependent properties are noted at regular intervals during the observation so they can easily be extrapolated to entire observation. The most common calibrations that are done once or twice during the entire observation (because of their almost time independent nature) are flux density, bandpass/delay, and polarization angle (per frequency setting and per correlator configuration). For other complex gain (amplitude and phase) the calibration intervals are decided based on weather conditions and baseline length. For example, for longer baselines (longer u-v distance and more important for high frequencies) the phase variations on the interferometers is often more than at the lower observing frequencies, therefore phase calibration is more frequent at higher frequencies. In gain calibration we often assume that the calibration solutions of the sky where the calibrator source is observed can be extrapolated over time and viewing angle. We also assume that the atmospheric conditions are almost same toward the sky of the target source. The other instrumental components like attenuators and requantizer are calibrated at the beginning of the observation[30].

The second important question comes - How to perform these calibrations? The most common method is to input a known signal to the instrument and analyse the output signal. The corrections are calculated by calibration measurements that need to be applied to output signal in order to get the true representation of input signal. A point source (simple and isolated) with known or assumed constant flux density and absolute sky position is typically observed to calibrate for the total observational response of an interferometer, but finding such special objects is extremely difficult and rare, hence VLA uses alternate sources that are almost point sources and dominate the observational response (the flux density may not be very constant) and are very common. These calibrators can be found on *VLA Calibrator List*[1].

Clearly, calibration is an integral part of observation to achieve our scientific goal therefore it must be planned thoughtfully and included in the observation time request proposal. This is the reason we purposefully devoted one - fourth time of observation in observing the flux, bandpass and phase calibrators (see Table 2.2). We will discuss these calibration steps in more detail with examples from our work.

2.2.2.1 Flux Calibration

The work of a correlator is to combine the the signals (at specific ν) into visibilities, however, it just processes the inputs that it gets from the electronic systems in terms of relative amplitudes and phases. Therefore these relative strengths must be readjusted to represent the flux density as measured from sky visibilities. At VLA for this purpose, we observe a flux calibrator for which the flux density at the observation frequencies is either known or assumed. Then during the post-processing steps we rescale the visibilities for this calibrator to the flux density for this frequency (by comparing with the observed data for that calibrator). Finally, with same setups the other visibilities (in same observation) can be matched using relative scale and absolute flux density of the calibrator. This scaled flux density will be used to determine the antenna gain amplitude g_i during complex gain calibration[30].

The flux density scales are determined using some standards, VLA uses Perley-Butler standard (2013, ApJS 204, 19) for all the observations done in 1 to 50 GHz. In CASA we used **setjy** task or this purpose. This would list all the available calibrators (in all VLA bands, A,C,K,L,Q,S,U,X) from the VLA calibrator list (such as 3C48, 3C147, 3C286 and

---

[1] Can be found at - `https://science.nrao.edu/facilities/vla/observing/callist`

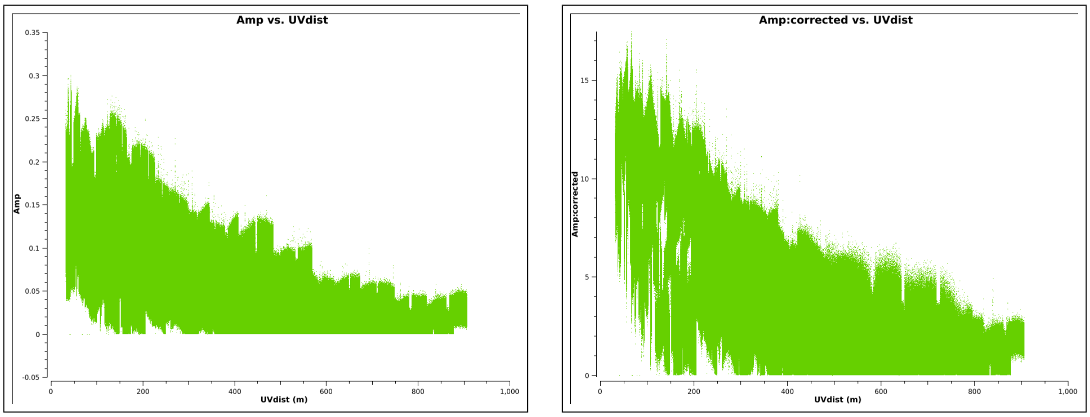

(a) Uncalibrated (unscaled) amplitude

(b) Calibrated (scaled) amplitude

Figure 2.4: 3c98 data before and after flux calibration.

3C138) and we can choose the best suited calibrators for our purpose. In our observation since we are searching for H I 21 cm line, we used L band that corresponds to 20 cm band in VLA. The flux calibrator used for our purpose is bright radio galaxy 3C147. The calibrated results can be seen in Figure 2.4.

2.2.2.2 Phase Calibration

This is an important calibration before the bandpass and delay calibration. The variations in phases are typically small but rapid so we average these variations in the bandpass. Solving phase variations is quite important as it prevents de-correlation when vector averaging of the data is done to calculate the bandpass solution. In CASA **gaincal** task is used for this purpose to solve for phase versus time for the central channels on our phase calibrator. A very important point to note here that, phase solutions are calculated with reference to a particular antenna and solutions for other antennas will be calculated relative to this reference antenna. Typically, we choose a central antenna, where the phase variations are minimum[30]. The phase calibration is performed by observing a near-by single calibrator and transferring the interpolated phases to the target field. In our observations we have used active galaxy J0409+1217 as phase calibrator. See Figure 2.5 for the results of phase calibration for our observation.

2.2.2.3 Bandpass and Delay Calibration

In mathematical words, with bandpass calibration we would solve for B_i of equation 2.3. First we do the delay calibration followed by the bandpass calibration. The small inaccuracies in antenna position, time etc. in correlator models can cause significant deviations from the model that are noticeable as a time-constant linear phase slope as function of frequency in the correlated data. To perform delay calibration we observe strong source in the sky to gain a high signal to noise ratio for the delay solution and

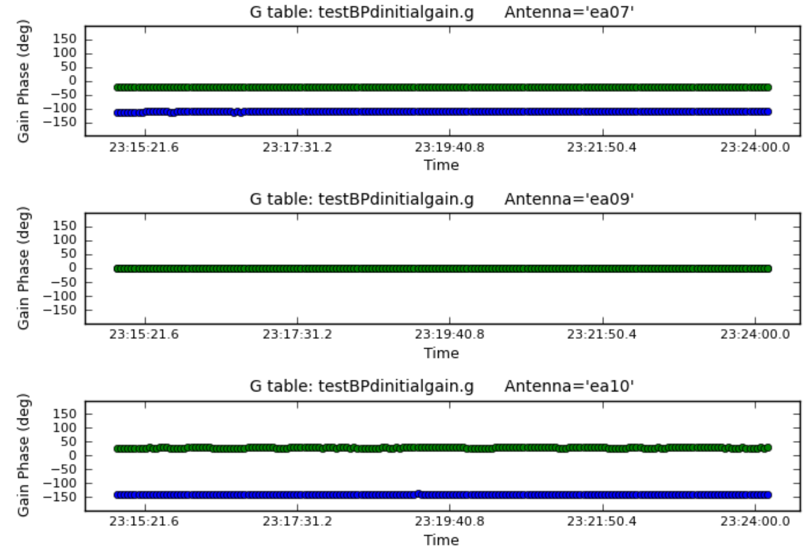

Figure 2.5: 3c98 phase calibration solution with reference antenna = ‘ea09’

neglect the time dependent variations. These slopes are called *delays* and are property of all spectral windows and can cause decorrelation of continuum signal and misrepresent the sky.

There are other impurities independent of delays such as - inaccuracies in frequency amplitudes and phase response as functions of frequency that need to be corrected. These corrections are also the property of subband and its location in baseband[30]. Ideally, the visibility data of bandpass calibrator should be constant with both frequency and baseline length. To correct for frequency is the actual aim of bandpass calibration. If bandpass is not corrected it would lead to incorrect relative amplitude and phase and give incorrect spectral representation of the sky. To perform bandpass and delay calibration we observe strong source in the sky to gain a high signal to noise ratio for the delay solution and neglect the time dependent variations. Alike delay calibration, the bandpass solutions are also determined on short time interval by observing a strong source in the sky, hence for both purposes we observe same source. A very typical and important property of bandpass solutions is that it should not add to the amplitude and phase of the noise in the image cube, it means that the S/N ratio of bandpass calibration is comparable or sometimes even better than the S/N ratio of flux density of target. Statistically, the noise is proportional to the product of inverse of the root of the bandwidth and the observation time (t_{obs}) this implies the calibration time (t_{cal}) should be larger than the product of observation time and square of ratio of fluxes of target (S_{target}) and flux calibrator (S_{cal}).

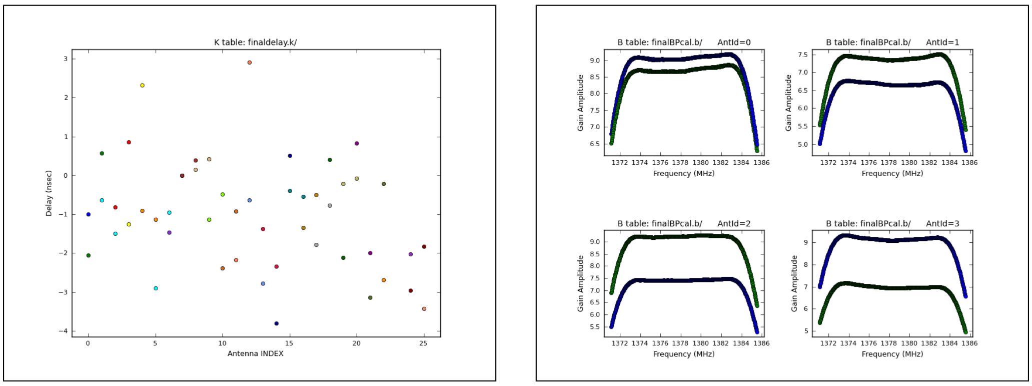

(a) delay solutions (within 4 ns)

(b) bandpass amplitude solutions

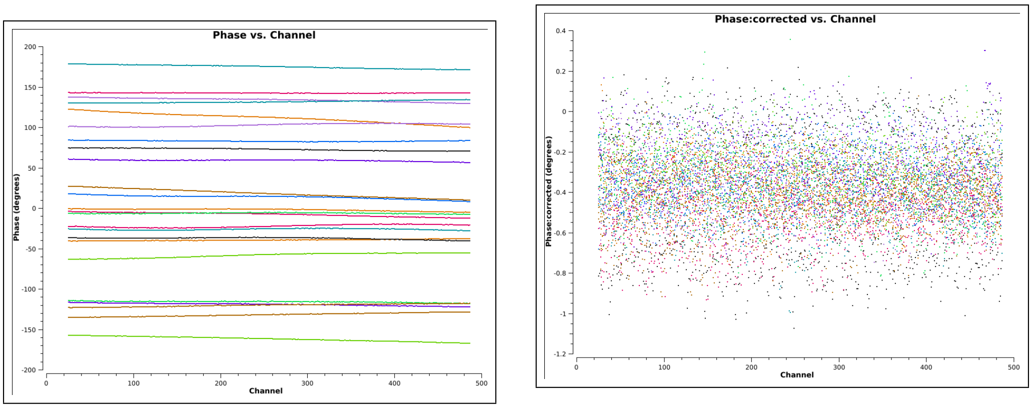

(c) delay before calibration (large variation)

(d) delay after calibration (variation removed)

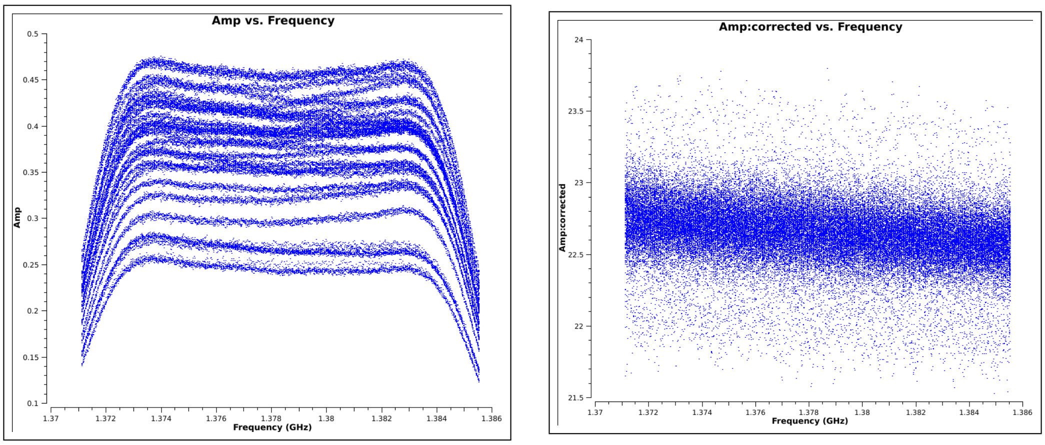

(e) Frequency dependent visibilities (before bandpass)

(f) Constant visibilities after bandpass calibration

Figure 2.6: 3c98 data before and after bandpass and delay calibration.

Mathematically, following relation should hold for bandpass calibration -

$$\mathrm{t_{cal}} > \mathrm{t_{target}} \cdot (\frac{\mathrm{S_{target}}}{\mathrm{S_{cal}}})^2 \tag{2.4}$$

Therefore, keeping above equation in mind we generally decide the time for which the bandpass calibrator is observed. The CASA tasks **gaincal** and **bandpass** are used for delay and bandpass calibrations respectively. Here also, a reference antenna is used for these both calibrations. The delay and bandpass solutions and calibrations can be seen in Figure 2.6.

2.2.2.4 Complex Gain Calibration

Till now, we have focused mainly on the time independent (static) calibration, where we have either scaled the fluxes (flux calibration) or determined the signal path properties that are largely constant for the observation (bandpass calibration). The complex gain calibration is performed to keep track of the properties that are time varying due to change in local conditions of instruments (such as receiver power level settings, corrupt baseband samplers). Mathematically, we are trying to find the solutions for g_i and θ_i in equation (2.3). As discussed above, the magnitude of the g_i is found with reference to the flux density calibrator. This calibration also takes care of the effect due to environment and atmosphere most prominently from the ionosphere at low frequencies and troposphere at high frequencies, signal interference from cellphones, digital camera, occasional solar flares, broadcasting satellite etc. The small variations can be corrected with proper gain calibration but larger variations like RFI can not be calibrated, in fact they need to be manually flagged from the data [30].

The gain calibrations are antenna based and assume that the variations in antenna gain are due to gradual change in amplitude and phase. This slow variation actually allows us to interpolate the variations by a smooth function that would image the true variation at the antenna. In order to determine the appropriate complex gain solutions for the target field we observe a gain calibrator (J0409+1217 for us) that is close to the target because if they are near enough then we can assume the atmosphere to be same along both directions (calibrator and target field). The observation is done on regular intervals to keep track of changes that it should not go far that its solutions can not be interpolated our target field. This is the reason we have observed complex gain calibrator J0409+1217 on regular intervals during our observation.The CASA task **gaincal** and **fluxscale** are used for this calibration. The results of complex gain calibration are shown in Figure 2.7.

2.2.3 Applying the Calibration

In the above sections the we have already applied all the calibrations to show the final results (see above figures). The main task in CASA used for applying all the calibrations that ares stored in calibration tables (like bandpass caltable (B), gain caltable (G), delay caltable (K)) is **applycal**. After applying the calibrations the calibrated data is stored as

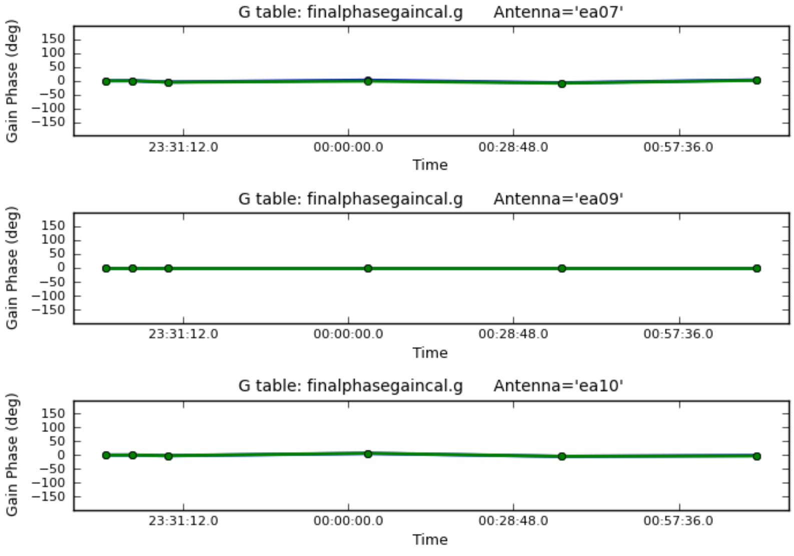

Figure 2.7: 3c98 complex gain calibration solution with reference antenna = ‘ea09’

corrected data, that would be further used for imaging purpose. One very important point is to note that if we find some more bad data after the calibration (each task has some limitations) we should manually flag them and recalibrate all the data again before imaging.

2.2.4 VLA CASA Calibration Pipeline

All these above mentioned steps can be performed manually in CASA, and sometimes may be more suitable, but in most cases they can be done via automatic programmes. VLA has developed CASA flagging and calibration pipeline[2] which comprise of several python written codes that automate all these steps and can perform most of the initial flagging and calibration part in a night. The manual processing can take more than a week. We used CASA pipeline for our flagging and calibration part for all the sources except 3c98 where we performed both pipeline and manual analysis to check the consistency between the results. Also note that the pipeline analysis should be done separately on all the spectral windows (in our case spw0 and spw1).

---

[2] CASA calibration pipeline can be found at - `https://science.nrao.edu/facilities/vla/data-processing/pipeline`

2.3 Imaging

Indeed, the flagging and calibration are an integral (and sometimes time consuming) part of any astronomical data analysis but they can not be the goal of an observation. The final aim of any astronomical observation is to make the image of the target field and process it to achieve our scientific goal. Mathematically, image (in sky plane) is just the 2D inverse Fourier transform of sky visibilities (in u-v plane) [31]-

$$\mathrm{I(l,m)} = \int\int \mathrm{V(u,v)e^{2\pi i(ul+vm)}du\,dv} \tag{2.5}$$

The above equation inherently neglects the w coordinate which is a good assumption at high frequencies. The CASA task **clean** and AIPS task **IMAGR** are used for imaging that perform two operations - Fourier transform of visibilities and deconvolution of resulting image. Equation (2.5) is the exact mathematical relation between these two, but in reality the imaging is much more complicated. We do not directly get the clean image $I(l,m)$ from inverse Fourier transform of $V(u,v)$, in fact we get a dirty image ($I^D(l,m)$) which is a complex convolution of true image and dirty beam ($s(l,m)$). Therefore deconvolution of dirty beam is required in order to get the clean image from the dirty image. Mathematically it can be understood as follows -

$$\mathrm{V(u,v)S(u,v)} \xrightarrow{\mathcal{F}} \mathrm{I^D(l,m) = I(l,m) \star s(l,m)} \xrightarrow{\text{deconvolution of s(l,m)}} \mathrm{I(l,m)}$$

$$\text{where, } \mathrm{s(l,m)} \xrightarrow{\mathcal{F}} \mathrm{S(u,v)}$$

In reality, these two tasks first analyze the $V(u,v)$ data by fitting some non linear models (for which noise properties are well defined) on our sampled visibilities then perform the Fourier transform on fitted $V(u,v)$ to get $I^D(l,m)$ and finally execute the final step of deconvolution of $s(l,m)$ from the dirty image to get the clean model components of $I(l,m)$. The imaging steps are explained pictorially in Figure 2.8. The two radio lobes of the galaxy can be seen in the cleaned image. The deconvolved (clean) images of other three galaxies are shown in Figure 2.9

2.4 Data Analysis in AIPS

After doing the initial flagging, calibration and continuum imaging part in CASA we split the target field from the calibrators as all the science part would be done with target field. This was done by **split** task in CASA, but since AIPS can only work with **fits** file we exported fits file using **exportuvfits** task in CASA. Once we had the required target **fits** file we moved to AIPS for further advance data analysis. The reason behind this step was to perform the continuum subtraction (i.e. removing the continuum part from the image to enhance the H I emission), which is much easier and more accurate in AIPS. The CASA is still under development so the imaging and continuum subtraction lack some credibility, on the other hand AIPS is quite old and much developed and tested for these purposes. The following AIPS steps were followed in our data analysis -

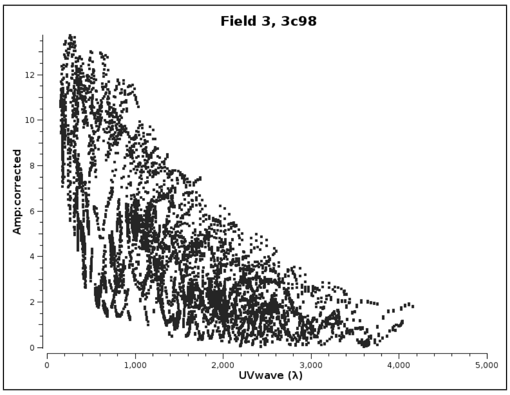

(a) corrected sky visibilities ($V(u,v)$)

$\downarrow\mathcal{F}$

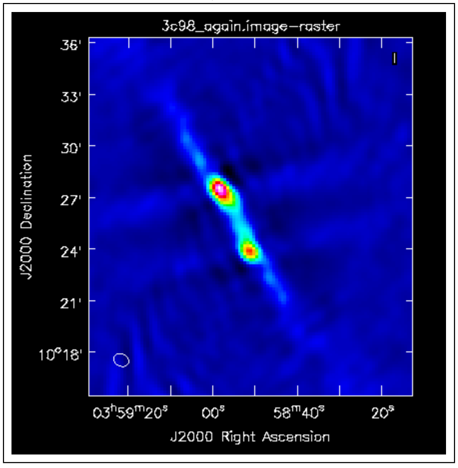

(b) dirty image ($I^D(l,m)$) of 3c98

$\downarrow$ *deconvolution*

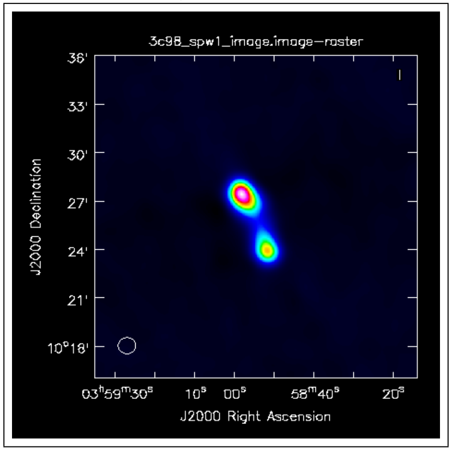

(c) cleaned image $I(l,m)$ of 3c98

Figure 2.8: Main steps in imaging of 3c98.

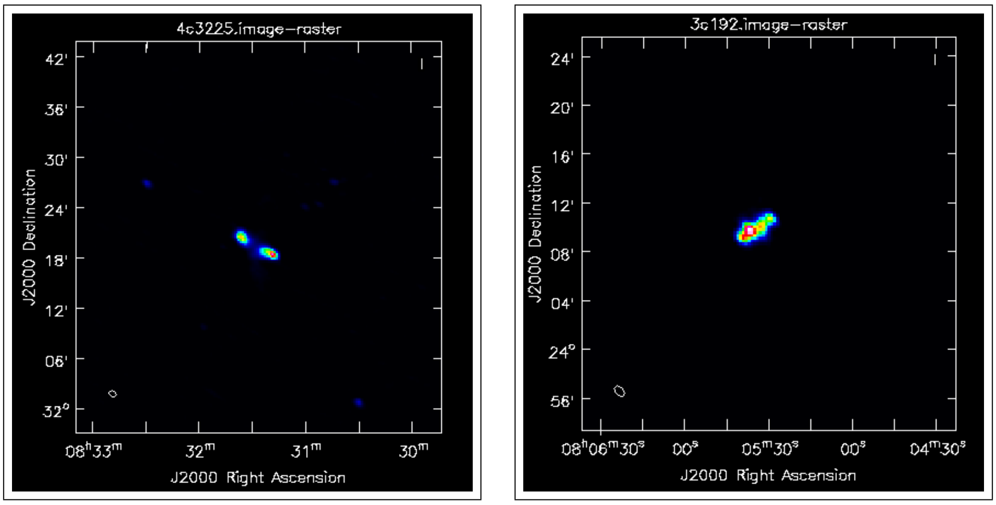

(a) cleaned image of 4c+32.25

(b) cleaned image of 3c192

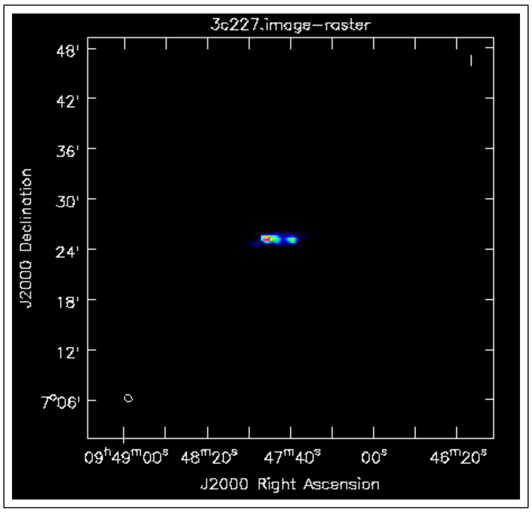

(c) cleaned image of 3c227

Figure 2.9: Cleaned image of our target radio galaxies.

- Loading the **fits** data in AIPS (with **FITLD**) and checking (with **UVPLT**) for any left bad data (like RFI spikes or bad channels), if found removed it with **WIPER** task.
- Used **SPLIT** task to averaged all 512 channels into a single channel by taking some channels from start and end (taking care that central channels where we expect emission are not used) and interpolating them to all the channels.
- Making of clean image (with **IMAGR**) of target field (split file should used). Some important parameters of imaging are tabulated in Appendix.
- Subtracted the continuum part from the clean image with **UVSUB** task, that brought down the total cleaned flux to almost one tenth of latter, that implied uvsub worked well.
- The object and earth are relatively moving so the emitted frequency is not the same as observed frequency, it is Doppler shifted and we need to correct for this effect. The emitted frequency also gets affected by earth rotation and position of antennas, they should also be corrected. These corrections are done by VLA Doppler shifting calculator fortran programme, **dopset**, that computes all these corrections based on the information of objects' redshifted frequency, RA, DEC, observation time and date and observatory's coordinates.
- Once we have the information of Doppler shifted frequencies we used it to shift the uv spectral line data set in frequency space. This was done with **CVEL** task. The task requires some careful entries of all the parameters. The main aim of this task is to shift all spectra to a given velocity and correct for effects of earth's rotation and its motion within the solar system. The task should be run on the continuum subtracted (**UVSUB**) file.
- The final step in imaging is to make the **image cubes** that store any information for emission as functions of RA, DEC and velocity (or frequency). The image cubes are made with same **IMAGR** but without any cleaning and averaging, therefore it looks gray and without continuum. The example can be seen in Figure 2.10.
- After completing all the imaging part, we move to our final goal, i.e. obtaining the spectra and search for H I emission. The next steps will be detailed in next section.

2.5 Obtaining the Spectrum

Imaging is the most important step in any data analysis and should be done with great care. The imaging steps and parameters are decided based on our science goal. Once the imaging part is well executed we can use those images to extract the spectra and search for the emission. There are some steps that need to be performed before extracting the spectrum from the 'spectral' image cubes, are explained below -

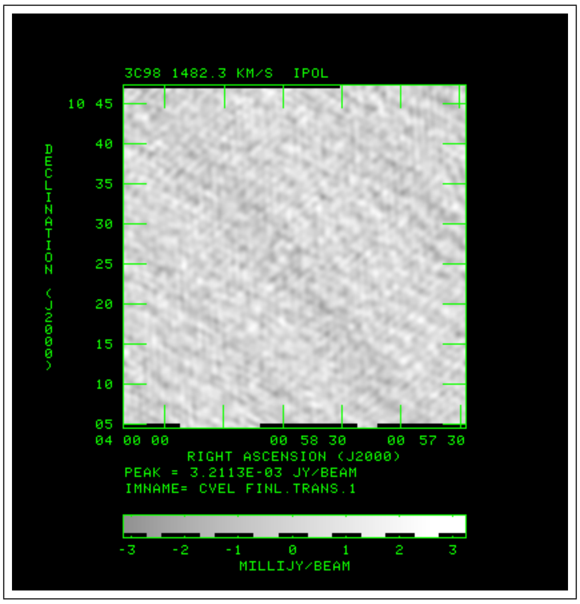

Figure 2.10: An image cube of 3c98 (continuum subtracted).

- The **UVSUB** task performs very well and removes most of the continuum emission from the cleaned image, but there are still some left over in the image cubes which need to be removed in order to get our spectral lines. The left over appears as slopes instead of a flat spectrum. This can be inspected with **ISPEC** task.
- The task that removes all these left over continuum emission is **IMLIN**. It uses some linear or non linear algorithms based on the parameters provided by user to remove and fit the continuum emission. In our case we have used linear fitting to remove the continuum emission. See Figure 2.11.
- IMLIN only works on the cubes where spectral axis (frequency) axis is the first axis and the two spatial coordinates are the second and third axes. This transposition is done with **TRANS** task with suitable transcod.
- Finally **ALTSWTCH** task is used to alter the frequency axis to velocity axis.

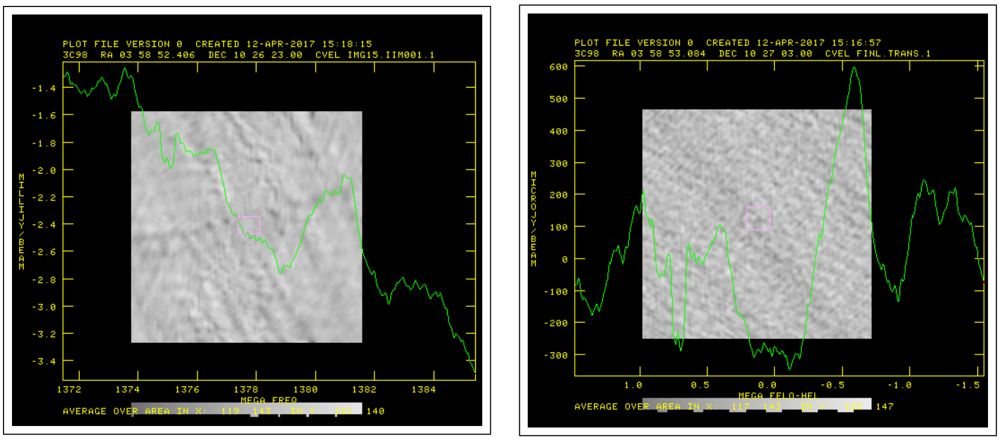

(a) 3c98 image cube without IMLIN

(b) 3c98 image cube after IMLIN

Figure 2.11: Continuum subtraction with IMLIN

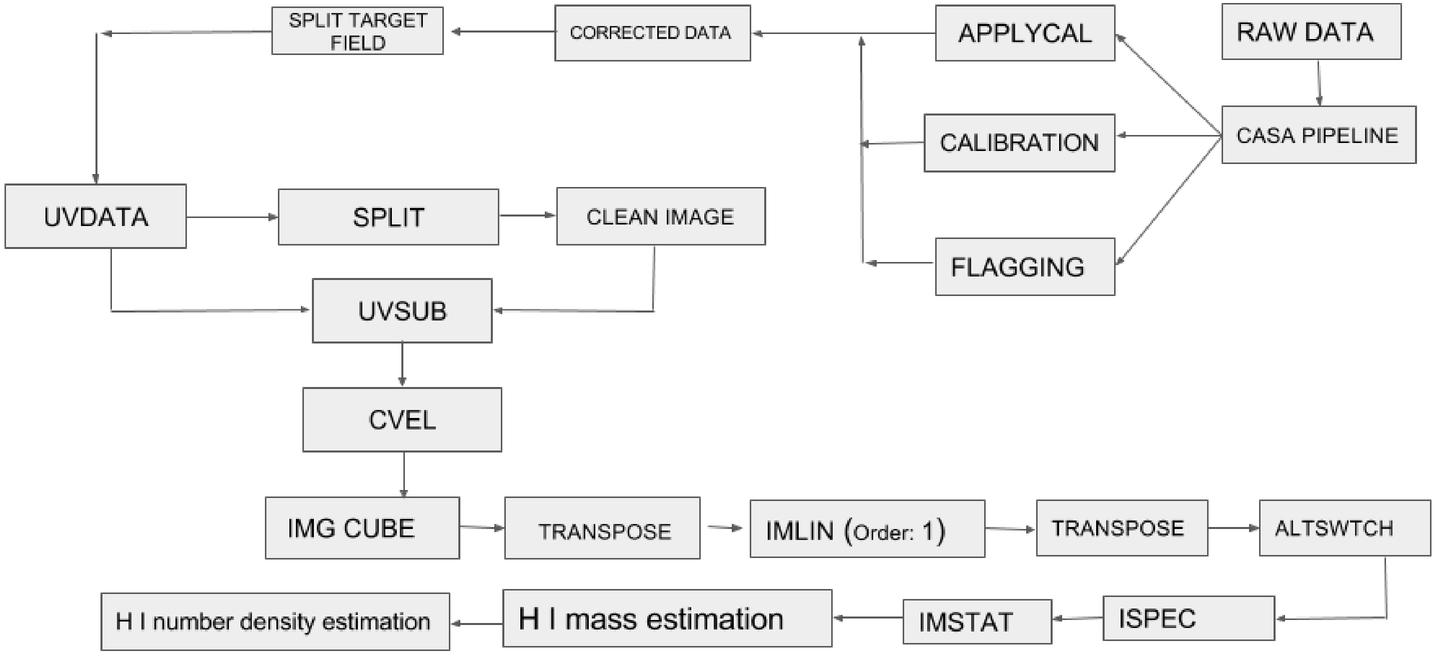

Figure 2.12: Flowchart of data analysis in CASA and AIPS.

Chapter 3

Results

In this chapter, we will present our results that we have obtained from our analysis. The first part will analyse the obtained spectra for all four sources and the next chapter will discuss the conclusion and future work.

3.1 Final Step in AIPS

After obtaining the image cubes and fitting their spectra (for removal of left over continuum emission) with IMLIN followed by altering the frequency axis to velocity axis in order to acquire the spectral lines as functions of velocity we need to detect the emission within a velocity width near the channels where the emission was expected. If there is any emission (or non-emission) the **rms** of the brightness in that region can be used to compute H I mass in that region. The rms is computed by task **IMSTAT** in AIPS. The main function of this task is to read a portion of an image and calculate the maximum and minimum brightness with mean and standard deviation (**rms**). The apertures can be chosen either rectangular or circular for selecting the portion of image.

3.2 Results for observed Radio Galaxies

As we have discussed in introduction in chapter 1 about our problem of searching for H I emission, now the obtained spectra for all sources will be presented along with the results in detail. The standard deviation in velocity for all sources were found to be similar as expected. While making the image cubes we averaged 15 channels together with a channel increment of 1. We were expecting emission from the central channels and this averaging allowed us to detect emission within a velocity width of 100 km s^{-1} if it was present. In case of non-detection with the IMSTAT computed **rms** noise we can calculate an upper limit on the H I mass and number density in the superdisk. The details of the rms noise, spectra and computed upper limits of H I mass and number density in 3σ rms noise limit, are presented separately for each source in the next sections. One very important point to make, although we had taken simultaneous observation in two spectral windows (spw0 and spw1) but we used only spw1 for our analysis once we compared the images for both subbands.

3.2.1 Computing H I Mass

Before applying the equation 1.4 to compute the H I mass we need to find all the parameters. To find these parameters we have followed some general mathematical steps for all the sources.

- The reported rms noise (flux) is in the unit **Jy/beam** but equation demands flux in **Jy** so we must find the number of beams available in the emission region. To calculate beam number we use following mathematical expressions-

  $$\text{Aperture size of superdisk, S} = \left(\frac{d}{D_A}\right) \cdot 206265 \text{ arcsec} \times \left(\frac{w}{D_A}\right) \cdot 206265 \text{ arcsec} \tag{3.1}$$

  where, d = diameter of superdisk (kpc), w = width of superdisk (kpc) and D_A = angular size distance (kpc). Also since 1 rad = 206265 arcsec it is multiplied to convert the size from *rad* to *arcsec.*

- Based on information such as - telescope angular resolution, pixel size, cell size etc. IMAGR also calculates the convolution size which is also the beam size of telescope (B) and can be found from image header, hence -

  $$\text{Number of beams available, n} = \frac{S}{B} \tag{3.2}$$

- RMS noise (flux) (Jy/beam) $\xrightarrow{\textit{multiply with } n}$ RMS noise (flux) (Jy)

3.2.2 Computing H I Number Density

Once the H I mass is estimated, we can immediately compute the number density (atoms per cm^3). We just need to follow some fundamental mathematical steps -

$$\text{Number of H I atoms, } \mathrm{N_H} = \frac{\mathrm{M_{H\,I}}}{\mathrm{m_H}} \Rightarrow \text{number density, } \mathrm{n_H} = \frac{\mathrm{N_H}}{\mathrm{V}}; \mathrm{V} = \pi \mathrm{r}^2 \cdot \mathrm{w} \tag{3.3}$$

where m_H is mass of H - atom and V is the volume of superdisk in cm^3 and $r = \frac{d}{2}$. The conversion of unit is -

$$1 \; kpc^3 = 2.94 \times 10^{64} \; cm^3 \tag{3.4}$$

3.2.3 Computing H I Column Density

Once the H I number density is estimated, we can immediately compute the column density (atoms per cm^2). We just need to follow one more fundamental mathematical step -

$$\text{H I column density, } \eta_{\mathrm{H\,I}} = \int_{\mathrm{LOS}} \mathrm{n_{H\,I}} \mathrm{ds} \Rightarrow \eta_{\mathrm{H\,I}} = \mathrm{n_{H\,I}} \int_{\mathrm{LOS}} \mathrm{ds} = \mathrm{n_{H\,I}} \cdot \mathrm{d} \tag{3.5}$$

where ds of size of object along line of sight (LOS) and the integral over LOS gives the diameter of the disk as we are observing disk edge-on.

3.2.4 Source 3c98

The first source that we analyzed was this radio galaxy. From the bandpass solutions shown in figure 2.6b we chose channels 31 to 490 for the average (over 15 channels with channel increment of 1) imaging as solutions are almost constant in this region. After making the image cubes and fitting with IMLIN we finally extracted the spectrum. We have not detected any emission within 100 km s^{-1} width of velocity near the central region (see Figure 3.1). In this non-detection case we report the **rms** noise of the region from where the emission was expected, and use it to calculate the upper limit of H I mass using equation 1.4 and H I number density from equation 3.3 in 3σ rms noise limit. The following table summarizes the parameters that we have used to estimate the upper limit of H I mass.

Table 3.1: 3c98 parameters [14] used to compute H I mass

d **(kpc)**	w **(kpc)**	D_A **(Mpc)**	D_L **(Mpc)**	S **(arcsec×arcsec)**	B **(arcsec×arcsec)**	n
30	15	126.5	134.3	48.91×24.46	56.34×46.71	0.45

From the analysis of our continuum subtracted image cubes of 3c98 we report the **rms** noise of 6.98×10^{-4} Jy/beam in the central region from where the emission was expected. Using above parameters and equation 1.4 we get H I mass-

$$\mathrm{M_{H\,I}} = 2.343{\times}10^5{\cdot}(1{+}0.030){\cdot}134.3^2{\cdot}3{\cdot}6.68{\times}10^{-4}{\cdot}0.45{\cdot}101.9\ \mathrm{M_\odot} = 4.2{\times}10^8\ \mathrm{M_\odot} \quad (3.6)$$

Hence, the number density and column density from equations 3.3 and 3.5 are -

$$\begin{aligned} \mathrm{N_{H\,I}} &= \frac{4 \times 10^8 \times 1.98 \times 10^{33}\ gm}{1.67 \times 10^{-24}\ gm} = 4.98 \times 10^{65} \\ \Rightarrow \mathrm{n_{H\,I}} &= \frac{4.98 \times 10^{65}}{\pi \cdot 15^2 \cdot 15 \cdot 2.94 \times 10^{64}} = 1.6 \times 10^{-3}\ atoms/cm^3 \\ \Rightarrow \eta_{\mathrm{H}} &= 1.6 \times 10^{-3}\ \cdot 30 \cdot 3.086 \cdot 10^{21}\ = 1.5 \times 10^{20}\ atoms/cm^2 \end{aligned}$$

3.2.5 Source 4c+32.25

From the bandpass solutions we chose channels 60 to 460 for the average (over 15 channels with channel increment of 1) imaging as solutions are almost constant in this region. After making the image cubes and fitting with IMLIN we finally extracted the spectrum. We have not detected any emission within 100 km s^{-1} width of velocity near the central region (see Figure 3.2). Here also we calculate the upper limit of H I mass using equation

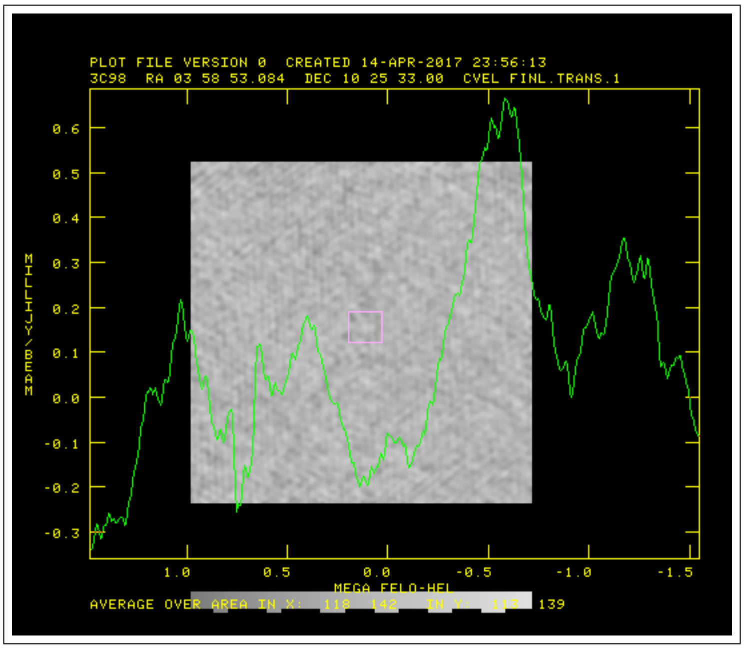

Figure 3.1: Spectra of 3c98, peaks are noise peaks, no detection.

1.4 and H I number density from equation 3.3 in 3σ rms noise limit. The following table summarizes the parameters that we have used to estimate the upper limit of H I mass.

Table 3.2: 4c+32.25 parameters [14] used to compute H I mass

d **(kpc)**	w **(kpc)**	D_A **(Mpc)**	D_L **(Mpc)**	S **(arcsec×arcsec)**	B **(arcsec×arcsec)**	n
150	52	207.5	229.3	149.11×51.69	55.16×41.52	3.36

From the analysis of our continuum subtracted image cubes for 4c+32.25 we report the **rms** noise of 3.986×10^{-4} Jy/beam. Using above parameters and equation 1.4 we get H I mass -

$$M_{H\,\mathrm{I}} = 2.343 \times 10^5 \cdot (1 + 0.0512) \cdot 229.3^2 \cdot 3 \cdot 3.986 \times 10^{-4} \cdot 104 \cdot 3.36 \ M_\odot = 5.41 \times 10^9 \ M_\odot \tag{3.7}$$

Hence, the number density and column density from equations 3.3 and 3.5 are -

$$N_{H\,\mathrm{I}} = \frac{5.41 \times 10^9 \times 1.98 \times 10^{33}\, gm}{1.67 \times 10^{-24}\, gm} = 6.41 \times 10^{66}$$
$$\Rightarrow n_{H\,\mathrm{I}} = \frac{6.41 \times 10^{66}}{\pi \cdot 75^2 \cdot 52 \cdot 2.94 \times 10^{64}} = 2.4 \times 10^{-4}\ atoms/cm^3$$
$$\Rightarrow \eta_{H\,\mathrm{I}} = 2.4 \times 10^{-4} \ \cdot 150 \cdot 3.086 \cdot 10^{21} \ = 1.1 \times 10^{20}\ atoms/cm^2$$

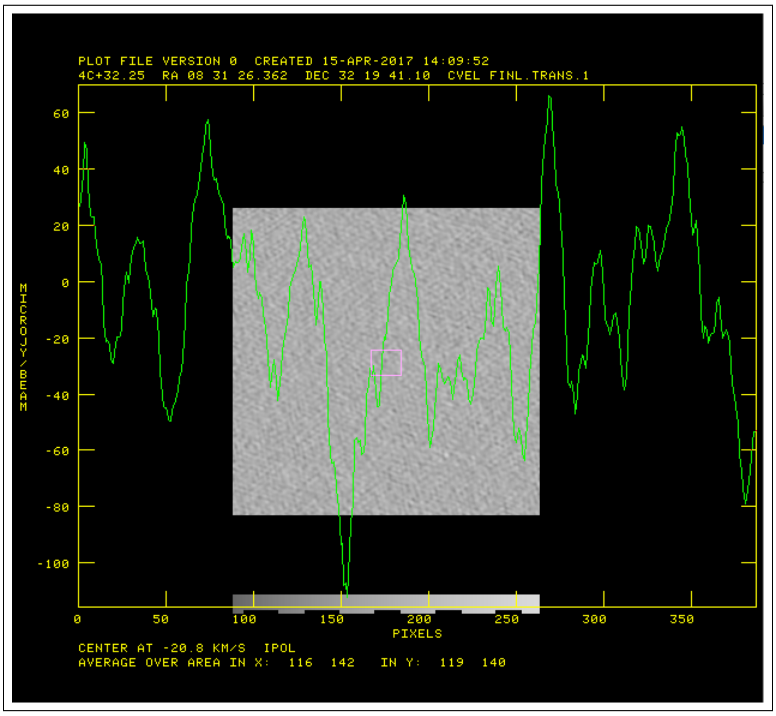

Figure 3.2: Spectra of 4c+32.25, peaks are noise peaks, no detection.

3.2.6 Source 3c192

From the bandpass solutions we chose channels 60 to 470 for the average (over 15 channels with channel increment of 1) imaging as solutions are almost constant in this region. After making the image cubes and fitting with IMLIN we finally extracted the spectrum. We have not detected any emission within 100 km s^{-1} width of velocity near the central region (see Figure 3.3). Here also we calculate the upper limit of H I mass using equation 1.4 and H I number density from equation 3.3 in 3σ rms noise limit. The following table summarizes the parameters that we have used to estimate the upper limit of H I mass.

Table 3.3: 3c192 parameters [14] used to compute H I mass

d **(kpc)**	w **(kpc)**	D_A **(Mpc)**	D_L **(Mpc)**	S **(arcsec×arcsec)**	B **(arcsec×arcsec)**	n
80	25	239.5	269	68.89×21.53	76.59×46.50	0.42

From the analysis of our continuum subtracted image cubes for 3c192 we report the **rms** noise of 4.56×10^{-4} Jy/beam. Using above parameters and equation 1.4 we get H I mass -

$$M_{H\,\mathrm{I}} = 2.343\times10^5\cdot(1+0.0597)\cdot269^2\cdot3\cdot4.56\times10^{-4}\cdot104.7\cdot0.42\ M_\odot = 1.1\times10^9\ M_\odot \quad (3.8)$$

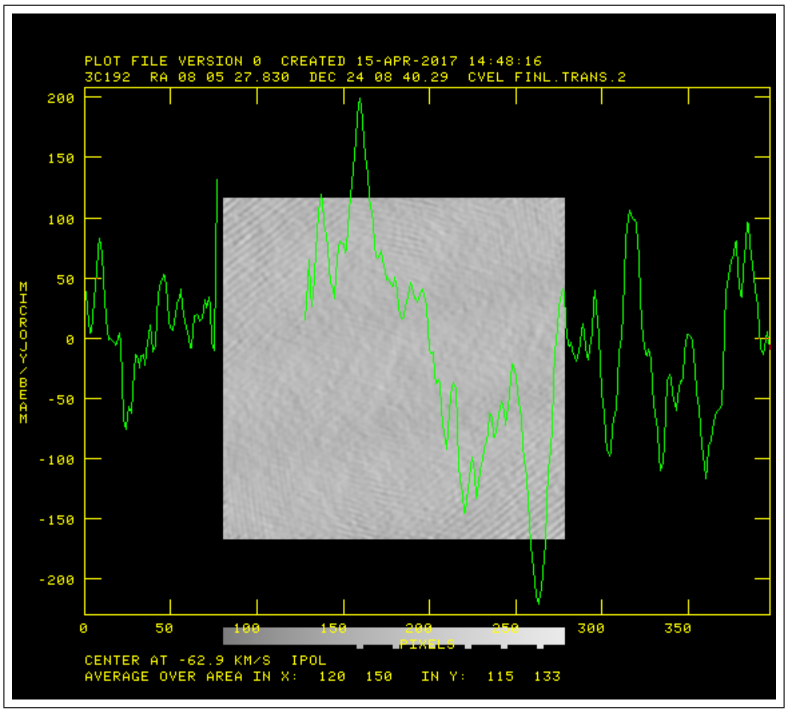

Figure 3.3: Spectra of 3c192, peaks are noise peaks, no detection.

Hence, the number density and column density from equations 3.3 and 3.5 are -

$$
\begin{aligned}
N_{H\,\mathrm{I}} &= \frac{1.1\times 10^{9}\times 1.98\times 10^{33}\ gm}{1.67\times 10^{-24}\ gm} = 1.3\times 10^{66}\\
\Rightarrow n_{H\,\mathrm{I}} &= \frac{1.3\times 10^{66}}{\pi\cdot 40^{2}\cdot 25\cdot 2.94\times 10^{64}} = 3.5\times 10^{-4}\ atoms/cm^{3}\\
\Rightarrow \eta_{H\,\mathrm{I}} &= 3.5\times 10^{-4}\ \cdot 80\cdot 3.086\cdot 10^{21}\ = 8.6\times 10^{19}\ atoms/cm^{2}
\end{aligned}
$$

3.2.7 Source 3c227

This analysis is little bit tricky because we have data for two different day observation. From the bandpass solutions we chose channels 60 to 460 for the average (over 15 channels with channel increment of 1) imaging as solutions are almost constant in this region for both day observation. After making the image cubes and fitting with IMLIN we finally extracted the spectrum (see Figure 3.4). Then we combined the spectra for further rms analysis. The way in which combined the spectra does make sure that the higher rms noise gets less weightage. The following table summarizes the parameters that we have used to estimate the upper limit of H I mass.

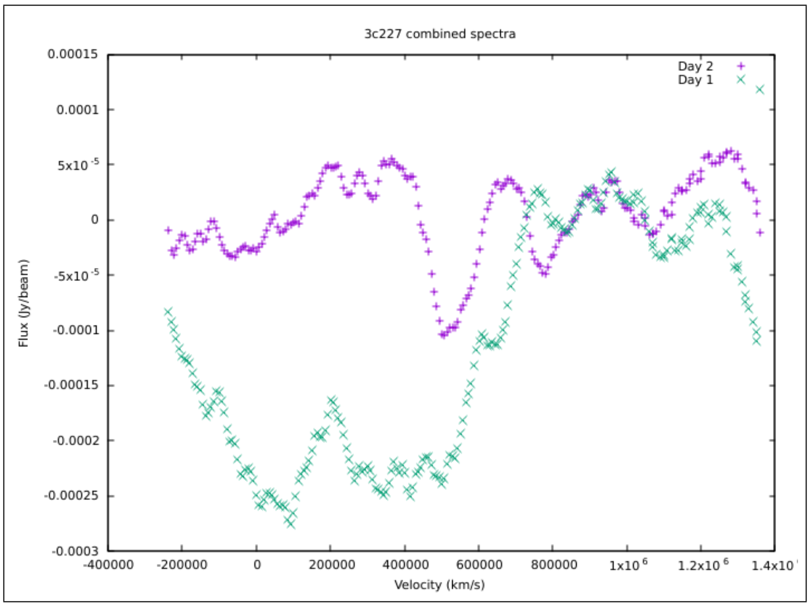

Figure 3.4: Spectra of 3c227, peaks are noise peaks, no detection.

Table 3.4: Combined 3c227 parameters [14] used to compute H I mass

d **(kpc)**	w **(kpc)**	D_A **(Mpc)**	D_L **(Mpc)**	S **(arcsec×arcsec)**	B **(arcsec×arcsec)**	n
85	33	334	393.8	52.49×20.38	59.51×50.74	0.35

To combine the spectra we used the weighted mean of two spectra as follows -

$$S_{eff} = f_1 S_1 + f_2 S_2;$$
$$f_1 = \frac{\frac{1}{\sigma_1^2}}{\frac{1}{\sigma_1^2} + \frac{1}{\sigma_2^2}} \;\&\; f_2 = \frac{\frac{1}{\sigma_2^2}}{\frac{1}{\sigma_1^2} + \frac{1}{\sigma_2^2}} \tag{3.9}$$

and with typical error propagation rules for weighted average quantities the 'effective noise rms' we get as -

$$\frac{1}{\sigma_{eff}^2} = \frac{1}{\sigma_1^2} + \frac{1}{\sigma_2^2} \Rightarrow \sigma_{eff} = \sqrt{\frac{\sigma_1^2 \cdot \sigma_2^2}{\sigma_1^2 + \sigma_2^2}} \tag{3.10}$$

From the analysis of our continuum subtracted combined image cubes of 3c227 we report $\sigma_1 = 1.2 \times 10^{-3}$ Jy/beam, $\sigma_2 = 9.5 \times 10^{-4}$ Jy/beam and **effective rms** noise of 7.45×10^{-4} Jy/beam. Using above parameters and equation 1.4 we get H I mass -

$$M_{H\,\text{I}} = 2.343 \times 10^5 \cdot (1 + 0.0858) \cdot 393.8^2 \cdot 3 \cdot 7.45 \times 10^{-4} \cdot 0.35 \cdot 107.4 \; M_\odot = 3.3 \times 10^9 \; M_\odot \tag{3.11}$$

Hence, the number density and column density from equations 3.3 and 3.5 are -

$$
\begin{aligned}
N_{H\,\mathrm{I}} &= \frac{3.3 \times 10^{9} \times 1.98 \times 10^{33}\, gm}{1.67 \times 10^{-24}\, gm} = 3.9 \times 10^{66} \\
\Rightarrow n_{H\,\mathrm{I}} &= \frac{3.9 \times 10^{66}}{\pi \cdot 42.5^{2} \cdot 33 \cdot 2.94 \times 10^{64}} = 3.8 \times 10^{-3}\, atoms/cm^{3} \\
\Rightarrow \eta_{H\,\mathrm{I}} &= 3.8 \times 10^{-3} \; \cdot 85 \cdot 3.086 \cdot 10^{21} \; = 9.9 \times 10^{20}\, atoms/cm^{2}
\end{aligned}
$$

3.3 A General Observation

From our analysis we calculate the upper limit of H I mass to be in the range of $10^{8} - 10^{9}$ $M_{\odot}$ for these superdisks, which is comparable to total H I content in our Milky Way. But due to extremely large sizes of the disks the number density of H I is quite low ($10^{-4} - 10^{-3}$) atoms per cm^{3}. The upper limits on column densities along the line-of-sight (assuming edge-on observation) lie in the range of $10^{19} - 10^{20}$ atoms per cm^{2}. A very important point to make is that they are very strong limits on mass, number density and column density. The results also indicate that the mixture of ionized, neutral and molecular gas are the major constituents of ‘superdisks’.

Chapter 4

Conclusion and Future Work

4.1 Conclusion

The H I 21 cm emission can provide some invaluable information about the intrinsic structure of these disks in way that has never been tried. In this effort to understand the nature of superdisk we have observed 4 nearby radio galaxies (with known superdisks) namely 3c98 (z = 0.030), 4c+32.25 (z = 0.0512), 3c192 (z = 0.0597) and 3c227 (z = 0.0858) with VLA for a sensitive search for H I emission. Due to limited time given on telescope and after the removal of RFI we have not detected any emission on the calibrated data within the velocity width of 100 km s^{-1} but we report the the upper limit on H I mass to lie between $4.2 \times 10^8 - 5.41 \times 10^9$ $M_\odot$ in 3σ rms noise limit. The following table summarizes the obtained results for H I mass and number density.

Table 4.1: Summary of upper limits on Mass, Number density and Column density of H I in 'superdisks'

Source	$\mathbf{M_{H\,I}}$ ($M_\odot$)	$\mathbf{n_{H\,I}}$ (cm^{-3})	$\eta_{H\,\mathrm{I}}$ (cm^{-2})	z
3c98	4.2×10^{8}	1.6×10^{-3}	1.5×10^{20}	0.0304
4c+32.25	5.4×10^{9}	2.4×10^{-4}	1.1×10^{20}	0.0512
3c192	1.1×10^{9}	3.5×10^{-4}	8.6×10^{19}	0.0597
3c227	3.3×10^{9}	3.8×10^{-3}	9.9×10^{20}	0.0858

Of course, these numbers are the upper limits on mass and density but they are very strong limits. If we compare masses with typical numbers in Milky Way like galaxy we find it to be very similar. But the number density is quite low in cmparison to normal galaxies because of the extremely large size of the superdisks. The low H I number density and intermediate column density very strongly indicate that most of the gas in 'superdisk' is in the ionized or molecular form or a mixture of them with this little amount of neutral hydrogen. This also suggests the possibility of some other large-scale structure that we still don't know. It would be exciting to observe some more RGs with ‘superdisks’ to answer this question.

4.2 Future Work

With a limited telescope time available to us we have not detected any emission and it indicates that we need to devote more observation time to these sources in order to obtain a strong and detectable emission. Apart from observing these four nearby galaxies we should also obtain some more examples of RGs that shows sharp emission gaps in their radio bridges. Such detection can be facilitated by sensitive low-frequency radio telescopes like GMRT. More optical surveys should be performed to understand the structure of superdisk in high-z RGs. The low number density of H I also indicates that major component of the disk is ionized or molecular gas and can therefore be studied by absorption spectra of the disk. On theoretical and computational hand high end simulations can done to understand the accretion of massive gaseous disks onto rapidly moving elliptical galaxies. The mechanism of heat transfer in such disks is very less studied and demands for a more careful and rigorous approach toward it. The understanding of the ultimate fate of superdisks over the cosmological time scale can also be a very interesting question (Gopal & Wiita 2000).

4.3 A Final Comment

The ‘superdisk’ postulate is quite well supported by observational evidences and can provide plausible explanations to several well observed phenomena such as - Laing-Garrington effect, the apparent asymmetry of Lyα emission and occurrence of absorption dips in high-z RGs, making them an object of great importance. The understanding of the nature of superdisks can therefore be an important research topic in attempt to bolster or discard this postulate, hence our analysis of these four nearby RGs can be the first and very significant step in this direction.

Appendices

Appendix A

Computing Image Parameters

Table A.1: Parameters for Imaging

Source	**Longest Baseline (kλ)**	**Cell Size (arcsec $\times$ arcsec)**	**Imsize (pixel $\times$ pixel)**
3c98	4.2	15 × 15	256×256
4c+32.25	4.3	14.3 × 14.3	256×256
3c192	4.4	14 × 14	256×256
3c227	4.0	15.7 × 15.7	256×256

To obtain a good quality image we can make the size of each pixel (CELLSIZE) 4 times less than the size of the beam. Mathematical prescription for calculating cellsize -

$$\text{beam size} = \frac{1.22\lambda}{B(\lambda)} \Rightarrow cellsize = \frac{\text{beam size}}{4} \tag{A.1}$$

where B is the longest baseline distance in wavelength unit.

References

[1] Bank, Jodrell & Leahy, J.P. 2003 vol. p. An Atlas of DRAGNs

[2] Baum, Stefi Alison; Heckman, Timothy M.; Bridle, Alan; van Breugel, Wil J. M.; Miley, George K. 1988, ApJS, 68, 643

[3] Black, A. R. S.; Baum, S. A.; Leahy, J. P.; Perley, R. A.; Riley, J. M.; Scheuer, P. A. G. 1992, MNRAS, 256, 186

[4] Blandford, R. D., & Rees, M. J. 1974, MNRAS, 169, 395

[5] Choudhuri, A.R., in Astrophysics for Physicists, Cambridge University Press 2010

[6] Clarke, D. 1996, in Energy Transport in Radio Galaxies and Quasars, ed. P. Hardee, A. Bridle, & A. Zensus (San Francisco : ASP), 311

[7] Colina, L., & de Juan, L. 1995, ApJ, 448, 548

[8] de Koff, S., et al. 1996, ApJS, 107, 621

[9] Draine, Bruce.T., in Physics of the Interstellar and Intergalactic Medium, Princeton University Press 2011

[10] Ellingson, E., Yee, H. K. C., & Green, R. F. 1991, ApJ, 371, 49

[11] Gallagher, John & Sparke, Linda, in Galaxies in the Universe: An Introduction, Cambridge University Press 2000.

[12] Garrington, S. T., Leahy, J. P., Conway, R. G., & Laing, R. A. 1988, Nature, 331, 147

[13] Garrington, S. T., Conway, R. G., & Leahy, J. P. 1991, MNRAS, 250, 171

[14] Gopal-Krishna, & Wiita, P. J. 2000, ApJ, 529, 189

[15] Gopal-Krishna, Giraud, E., Melnick, J., & della Valle, M. 1995, A&A, 303, 705

[16] Goudfrooij, P. 1994, Ph.D. dissertation, Univ. Amsterdam

[17] Hooda, J. S., & Wiita, P. J. 1996, ApJ, 470, 211

[18] Laing, R. A. 1988, Nature, 331, 149

[19] Leahy, J. P., & Perley, R. A. 1991, AJ, 102, 537

[20] Leahy, J. P., & Williams, A. G. 1984, MNRAS, 210, 929

[21] McCarthy, P. J., Baum, S. A., & Spinrad, H. 1996, ApJS, 106, 281

[22] McCarthy, P. J. 1993, ARA&A, 31, 639

[23] McCarthy, P. J., Spinrad, H., van Breugel, W., Liebert, J., Dickinson, M., & Eisenhardt, P. 1990, ApJ, 365, 487

[24] Norman, M. L. 1996, in Energy Transport in Radio Galaxies and Quasars, ed. P. Hardee, A. Bridle, & A. Zensus (San Francisco : ASP), 319

[25] Scheuer, P. A. G. 1974, MNRAS, 166, 513

[26] Sparks, W. B., Macchetto, F., & Golombek, D. 1989, ApJ, 345, 153

[27] Spinrad, H. 1989, in The Epoch of Galaxy Formation, ed. S. Frenk et al. (Dordrecht : Kluwer), 59

[28] van Ojik, R., Röttgering, H. J. A., Carilli, C. L., Miley, G. K., & Bremer, M. N. 1996, A&A, 313, 2

[29] Verschuur, G.L. & Kellermann, K.I., in Galactic and Extragalactic Radio Astronomy, Springer 1988

[30] VLA Calibration Tutorial: `https://science.nrao.edu/facilities/vla/docs/manuals/obsguide/calibration`

[31] VLA Imaging Tutorial: `https://casaguides.nrao.edu/index.php/VLA_Continuum_Tutorial_3C391-CASA4.6`

[32] CASA Documentation: `https://casa.nrao.edu/`

[33] AIPS Documentation: `http://www.aips.nrao.edu/index.shtml`

[34] Essential Radio Astronomy: `https://science.nrao.edu/opportunities/courses/era`